Geochemical Perspectives Letters

The key role of bedrock composition in the formation of carbonates on Mars

C. Gil-Lozano[1,2*], F. Baron[3], A. Gaudin[1], J.-P. Lorand[4], V. Fernandez[5], J. Hamon[5], N. Mangold[1]

https://doi.org/10.7185/geochemlet.2403

Abstract

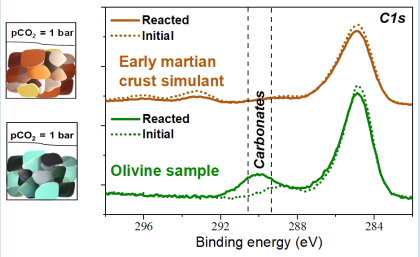

Martian carbonates are fundamental minerals for understanding the geochemical and climatic evolution of the planet and the search for potential life, representing one of the key objectives for the Perseverance rover at Jezero Crater. However, the scarcity of carbonate reservoirs on the surface compared to the extent of terrestrial carbonates questions whether these carbonates are indicators of past surface conditions or products from deeper processes unrelated to martian climate. We investigate the formation of carbonates by surface weathering under a CO_2 atmosphere in a suite of individual minerals and martian simulants based on the early Mars crust composition. We identify the formation of magnesium carbonates in olivine-bearing samples, but not in the early martian crust simulants. These findings are consistent with the association of carbonates with olivine-rich substrate detected on Mars and highlight the role of the substratum composition in the distribution of carbonates formed by surface processes. Hence, we conclude that the limited surface reservoirs of carbonate are reconcilable with the existence of a CO_2-rich atmosphere on early Mars.

Received 18 May 2023 | Accepted 19 December 2023 | Published 25 January 2024

Introduction

Carbonates on Mars are reported from orbital, *in situ*, and martian meteorite studies. Apart from minor carbonates (<5 wt. %) identified within more recent polar terrains (Boynton *et al.*, 2009) and the carbonate compounds identified in three nakhlite meteorites (Bridges *et al.*, 2019), these carbonates are inferred to have formed during the Noachian epoch (*i.e.* >3.6 Ga). Indeed, the largest known carbonate-bearing unit, at Nili Fossae, is inferred to be pre-Hesperian in age (~3.8 Ga; Mandon *et al.*, 2020). Hypotheses for the formation of the Nili Fossae carbonates include both local hydrothermalism (Mangold *et al.*, 2007; Ehlmann *et al.*, 2009), and regional weathering (Ehlmann *et al.*, 2009), which is consistent with the persistence of fluvial activity in the region (Mangold *et al.*, 2007) and the inferred lacustrine precipitation of carbonates in the Jezero Crater (Horgan *et al.*, 2020). Similarly, the carbonate concretions in the ALH84001 meteorite, which formed at ~3.9 Ga, originated from cool water (18 ± 4 °C) that had interacted with atmospheric CO_2 (Halevy *et al.*, 2011). These observations indicate that carbonate minerals likely formed at, or near, Mars' surface during its early history, coinciding with the development of fluvial valleys and deep weathering profiles. These findings suggest that Mars experienced a warmer and wetter climate in its early history, likely sustained by a thicker CO_2 atmosphere. Indeed, the MAVEN's observations show a significant loss of Mars's atmosphere (<0.8 bar CO_2) in its early history (Jakosky *et al.*, 2018). Therefore, the observational evidence from both the surface and the upper atmosphere points toward extensive interactions between the early Martian crust, an active hydrosphere, and a thicker CO_2 atmosphere.

Climatic conditions in this early Mars could have induced abundant carbonate precipitation in near surface environments. However, orbiting near-infrared spectrometers primarily detect phyllosilicates and sulphates among alteration minerals, whereas carbonate minerals are relatively rare (Carter *et al.*, 2023). Keep in mind that the identification of minerals by remote sensing spectra can be obscured by dust. The scarcity of large carbonate reservoirs could be explained by an acidic period in the Hesperian age that prevented their formation and dissolved those previously formed. However, the extension and age of Nili Fossae carbonates contradict such a hypothesis.

The overall composition of Mars' bedrock is commonly inferred to be basaltic and olivine-rich (olivine > 20 wt. %) (*e.g.*, McSween *et al.*, 2006). However, recent analyses of igneous rocks from the ancient bedrock surrounding Gale Crater (Mangold *et al.*, 2016) and of ancient Martian meteorites (Hewins *et al.*, 2017) suggest that felsic and alkali-rich rocks

1. LPG, Nantes Université, Université Angers, Université Le Mans, CNRS, UMR 6112, Nantes, France
2. Centro de Investigación Mariña, XM1, Universidade de Vigo, 36310 Vigo, Spain
3. Université de Poitiers, CNRS, IC2MP, Poitiers, France
4. Institut de Mineralogie, Physique de la Matière et Cosmochimie, UMR CNRS 7590, Sorbonne Université and Muséum National d'Histoire Naturelle, 61 Rue Buffon, 75005 Paris, France
5. Institut des Matériaux Jean Rouxel (IMN), CNRS/Université de Nantes, Nantes, France
* Corresponding author (email: carolina.gil.lozano@uvigo.gal)

Table 1 Summary of the samples analysed in this study. The bulk chemical composition of martian simulants samples was estimated according to the proportion of the minerals used (Baron *et al.*, 2019).

Individual minerals	Structural formula
Mg-olivine (Fo_{92})	$Al_{0.01}Mg_{1.78}Fe_{0.16}\ Si_{1.05}\ O_4$
Ferroan olivine (Fo_{65})	$Mg_{1.30}Fe_{0.70}\ Si_{1.00}\ O_4$
clinopyroxene (augite)	$Na_{0.09}Ca_{0.58}Al_{0.19}Mg_{0.92}Fe_{0.21}\ Si_{1.92}Al_{0.08}\ O_6$
plagioclase (An_{60})	$K_{0.01}Na_{0.39}Ca_{0.60}\ Al_{1.53}Mg_{0.01}Fe_{0.01}Si_{2.44}\ O_8$
K-feldspar (Or_{85})	$K_{0.85}Na_{0.15}\ Al_{0.97}Mg_{0.01}Fe_{0.01}\ Si_{3.01}\ O_8$

Martian crust simulants	Minerals (wt. %)		Chemical Compositions (wt. %)	
Martian crust simulant-O (Sim-O)	Ferroan olivine ($Mg_{1.30}Fe_{0.70}\ Si_{1.00}O_4$)	11.8	SiO_2	52.5
	Orthopyroxene ($Na_{0.03}Ca_{0.04}Al_{0.08}Mg_{1.58}Fe_{0.27}Si_{2.01}O_6$)	17.7	Al_2O_3	13.3
	Clinopyroxene ($Na_{0.09}Ca_{0.58}Al_{0.19}Mg_{0.92}Fe_{0.21}Si_{1.92}Al_{0.08}O_6$)	23.5	FeO	6.9
	Plagioclase ($K_{0.01}Na_{0.39}Ca_{0.60}Al_{1.53}Mg_{0.01}Fe_{0.01}Si_{2.44}O_8$)	32.4	MgO	13.2
	K-feldspar ($K_{0.85}Na_{0.15}Al_{0.97}Mg_{0.01}Fe_{0.01}Si_{3.01}O_8$)	12.8	CaO	8.4
	Apatite ($Ca_{4.67}Na_{0.08}Mg_{0.04}(P_{2.85}Si_{0.06}O_4)_3F_{1.21}Cl_{0.06}$)	2	Na_2O	2.0
			K_2O	1.9
			P_2O_5	1.7
Martian crust simulant-M (SIM-M)	Magnetite (Fe_3O_4)	10.9	SiO_2	49.3
	Orthopyroxene ($Na_{0.03}Ca_{0.04}Al_{0.08}Mg_{1.58}Fe_{0.27}Si_{2.01}O_6$)	17.8	Al_2O_3	13.7
	Clinopyroxene ($Na_{0.09}Ca_{0.58}Al_{0.19}Mg_{0.92}Fe_{0.21}Si_{1.92}Al_{0.08}O_6$)	23.7	FeO	12.9
	Plagioclase ($K_{0.01}Na_{0.39}Ca_{0.60}Al_{1.53}Mg_{0.01}Fe_{0.01}Si_{2.44}O_8$)	32.7	MgO	9.6
	K-feldspar ($K_{0.85}Na_{0.15}Al_{0.97}Mg_{0.01}Fe_{0.01}Si_{3.01}O_8$)	12.9	CaO	8.6
	Apatite ($Ca_{4.67}Na_{0.08}Mg_{0.04}(P_{2.85}Si_{0.06}O_4)_3F_{1.21}Cl_{0.06}$)	2	Na_2O	2.1
			K_2O	2.0
			P_2O_5	1.8

are more abundant in the Mars' ancient crust than initially presumed (Sautter *et al.*, 2016). Therefore, most carbonates >3.6 Ga old may have been formed from the alteration of this ancient crust, and not from the post-Noachian basaltic plains. In this study, we investigate the role of the bedrock compositions on the formation of carbonate by aqueous alteration. In prior experiments simulating early Mars conditions ($pCO_2 = 1$, T = 45 °C), moderate (Gaudin *et al.*, 2018) to minor magnesium carbonates (Dehouck *et al.*, 2014) were identified from forsteritic-olivine (Fo_{90}) weathering. However, Fourier transform infrared spectroscopy (FTIR) showed no carbonate detection (>~0.8 wt. %) in less magnesian olivines under similar geochemical conditions (pCO_2 from 0.1 to 1 bar, T = 25 °C; Kissick *et al.*, 2021). These weathering experiments focused on olivine minerals alone. Here, we experimentally investigate the reactions of a range of potential crustal compositions (*e.g.*, from ultramafic to more felsic composition) on carbonate formation under a thick CO_2 atmosphere (1 bar). The initial materials cover various individual silicate minerals including two types of olivine (Fo_{92} and Fo_{65}) to assess differences between the Mg-rich forsterite with the more Fe-rich forsterite identified at Nili Fossae (Brown *et al.*, 2020), pyroxenes, and feldspars. We also analyse two synthetic ancient crust samples based on the chemical composition of the NWA 7533 and NWA 7034 martian regolith breccias (*e.g.*, Hewins *et al.*, 2017) and the more alkali-rich composition of the early Mars crust identified in conglomerates in Gale Crater (Mangold *et al.*, 2016) (Table 1). To explore the influence of olivine concentration, we added Fo_{65} (~11.8 wt. %) to the crust simulant-O (Sim-O), whereas the simulant-M (Sim-M), contains magnetite but no olivine. The description of the experimental set up (Fig. S-1) and the chemical proprieties of the experimental solutions (Fig. S-7) have been reported by Baron *et al.* (2019). Here, we investigate the potential carbonate occurrences in the altered solids. Aiming to analyse the surface alteration of the samples, we used X-ray Photoelectron Spectroscopy (XPS) (sampling depth between 3–10 nm) in addition to the more conventional FTIR.

Results

We estimate the atomic percentages of the elements on the samples' surfaces by analysing XPS survey spectra (Fig. S-2). Then, we fit the binding energy of the core level *C1s* feature to identify the specific carbonate species (Fig. 1). In this energy range, all samples exhibit the usual contribution of ubiquitous adventitious carbon resulting from hydrocarbon physisorption onto surfaces. The primary peak of this adventitious carbon, denoted as C-H, occurs at 284.8 eV, while the carbonate peak (CO_3) emerges around ~289.7 eV, depending on the ionic character of the metal-carbon bond (*e.g.*, $MgCO_3$ ~290 eV and $CaCO_3$/$FeCO_3$ ~289.5 eV). All the unreacted samples (*i.e.* fresh material before reaction) except potassium feldspar (K-spar), show minor contribution from carbonate. However, only the reacted olivine-bearing samples (Fo_{92} and Fo_{65}) show a substantial increase of a well resolved carbonate peak around 290 eV, which represents Mg-CO_3 groups (Fig. 1, extended Fig. S-3 and Table S-1).

Figure 2 depicts the amount of carbonate at mineral surfaces before and after reactions together with the final pH values of the solutions. High pH values result from the weathering of mafic minerals (*i.e.* olivine and pyroxene), which neutralise the acidity derived from a CO_2-rich atmosphere ($pH_0 \sim 3.6$); the solutions with lower pH values reflect the hydrolysis of felsic minerals (*i.e.* feldspars). Solutions from the martian simulants also have low pHs because they contain abundant feldspars. Only the olivine samples (Fo_{92} and Fo_{65}) formed substantial proportions of carbonates during reaction, and only their solutions had pH > 6.2, the threshold for carbonates formation under a $pCO_2 = 1$ bar atmosphere (Bullock and Moore, 2007). Mg-rich olivine (Fo_{92}) produced higher carbonate formation than Fe-rich

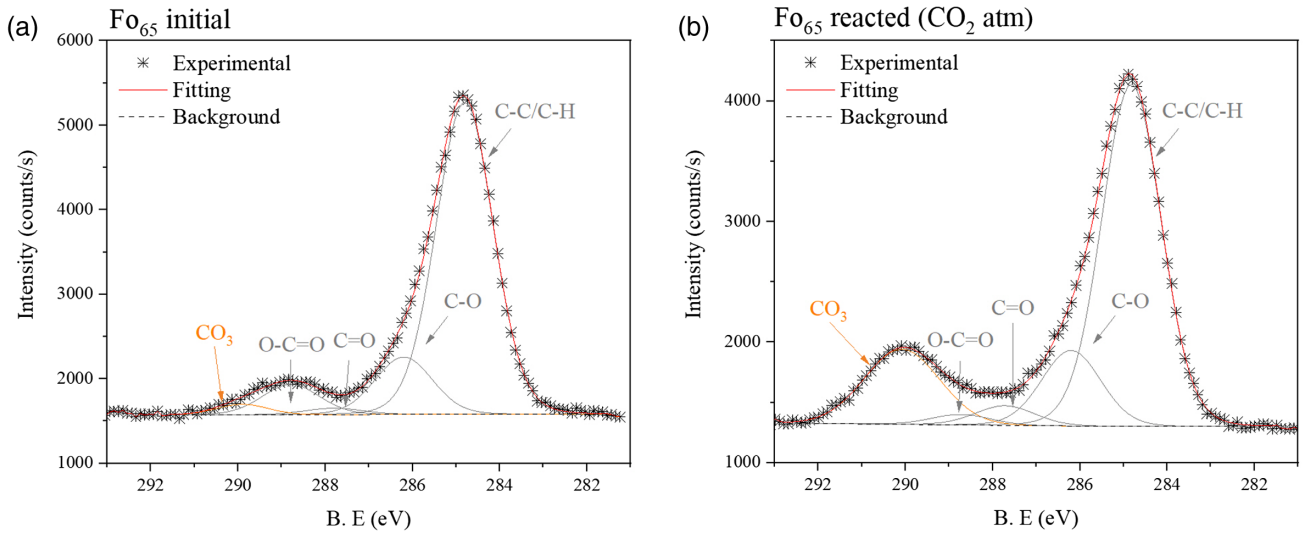

Figure 1 Fitting model of the *C1s orbital* for Fo_{65} sample, **(a)** initially, and **(b)** after reaction (under CO_2 atmosphere) (see SI for spectra deconvolution).

olivine (Fo_{65}). Conversely, potassium feldspar (K-spar) lacked carbonates and yielded the lowest pH solution (pH ~ 4.75). Simulant samples (Sim-O and Sim-M) did not show either a significant increase in carbonate compounds, nor appreciable differences between them, despite the presence of olivine in Sim-O (Fo_{65} ~ 11.8 wt. %) and their differences in the iron and magnesium content.

Figure 3 shows the magnesium high resolution XPS spectra (*Mg2p* orbital) of the olivine and Sim-O samples. When comparing initial and reacted samples, we only identified a change in the magnesium peak of olivine samples. This change manifests as a shift towards higher binding energies and an asymmetric broadening, a feature not observed in Sim-O. This change suggests the presence of $MgCO_3$ (~50.6 eV), consistent with the carbonate peak position identified in their *C1s* spectra (*i.e.* 290 eV ~$MgCO_3$).

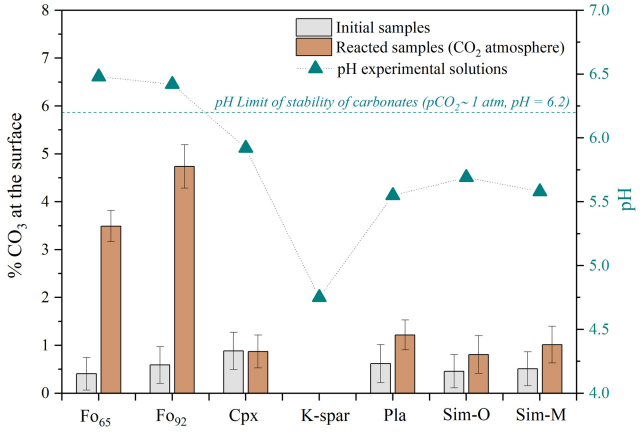

Figure 2 Amount of carbonate in the samples (bars) and pH value (triangles) of the solutions at the end of the experiment (see SI for % calculations). The error bars show the uncertainty of the carbon estimation associated with the survey quantification (standard deviation in Fig. S-2). The $pH_0 = 3.6$, corresponding to the pure water equilibrated with the $pCO_2 = 1$ bar. The dashed line marks the pH threshold of carbonates stability for $pCO_2 = 1$ bar (Bullock and Moore, 2007).

We also examined FTIR spectra for signatures of carbonate minerals. The bulk samples (*i.e.* whole size fractions) showed no features assignable to carbonate minerals, because of their low degree of alteration. However, the finest size fractions (<1 μm), did show absorptions from the strongest vibrational IR band for carbonates (*i.e.* the asymmetric stretching mode [$v_3(CO_3)$]) in several samples (Fig. S-4). The intensity of this band in reacted olivine samples suggests that carbonate formed during reaction, in agreement with the XPS results (Fig. 2). FEG-SEM images also suggest the presence of small particles of carbonate minerals, inferred by their crystal shape, on olivine samples (Fig. S-5). Note, however, that we cannot directly use the carbonate IR band intensity as a measure of carbonate abundances because it is only apparent in the size fraction <1 μm. The spectra enlargement (2000–600 cm^{-1}) of olivine samples shows that $v_3(CO_3)$ feature is split into two barely resolved peaks, which match well with a hydrated magnesium carbonate (*e.g.*, hydromagnesite; Fig. S-6). The saturation indices of carbonates calculated from the chemistry of experimental solutions (Figs. S-7, S-8) (Baron *et al.*, 2019) are also consistent with the solid products identified in this study. However, the use of this variable to predict mineral formation should be employed with caution (see geochemical modelling and carbonates in SI).

Discussion

Our weathering experiments under early Mars-like conditions show that, among potential materials of the early Mars crust, only olivine (Fo_{92} and Fo_{65}) reacts to form significant proportions of carbonate minerals (Fig. 1). Carbonation resulting from ultramafic rock reaction has been extensively studied as a $CO_{2(g)}$ capture strategy on Earth (*i.e.* high T and/or high P conditions) because it can neutralise the acidity imposed from CO_2 dissolution (Snæbjörnsdóttir *et al.*, 2020). The pH values of our post-reaction solutions show that under early Mars-like conditions, this neutralisation is particularly effective in olivine samples (Fig. 2), where we identify the formation of Mg carbonates (Figs. 1, 3 and Figs. S-3, S-6). The formation of magnesite is usually linked to elevated temperatures (T > 50 °C) due to the high hydration energy of Mg^{2+}. However, hydrated Mg carbonates can form in solutions with a high concentration of Mg^{2+} under near ambient temperatures (Gaudin *et al.*, 2018), as shown by our XPS and FTIR spectra (Figs. 1, 3 and Figs. S-3,

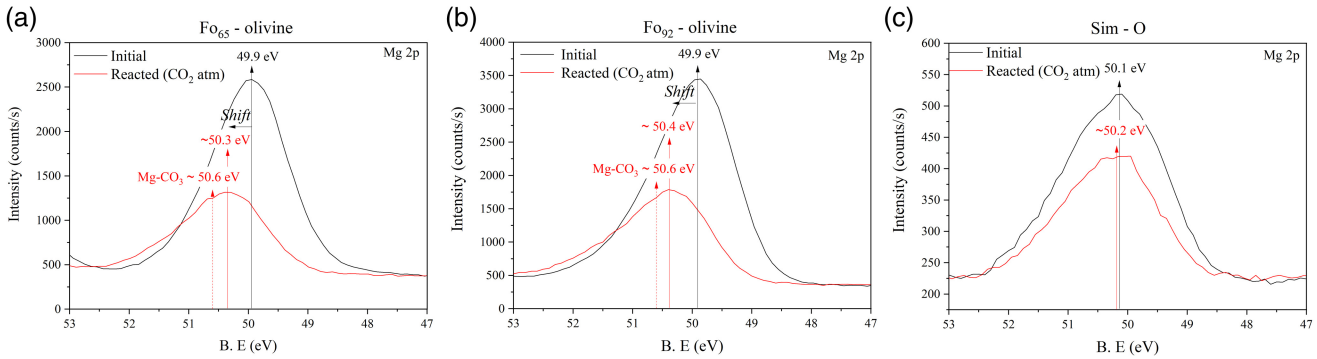

Figure 3 *Mg 2p* high resolution XPS spectra before (black colour) and after reaction under a CO_2 atmosphere (red colour) of **(a)** Fo_{65}-olivine, **(b)** Fo_{92}-olivine, and **(c)** simulant sample with Fo_{65} (Sim-O). The solid arrows (black colour) mark the position of the main peak of the unreacted samples whereas dashed arrows (red colour) mark the position of the $MgCO_3$ peak.

S-6). Then, this hydrated precursor can turn into anhydrous magnesite as occurs in low temperature evaporitic environments on Earth (*e.g.*, Scheller *et al.*, 2021). This geological scenario could explain the formation of carbonates identified (from orbit) along the margins of the Jezero (playa) lake (Horgan *et al.*, 2020), setting aside the specific interferences that the development of passivation layers may cause on olivine carbonation rates (Oelkers *et al.*, 2018 and references therein). Interestingly, we do not identify siderite, not even in the iron-rich forsterite (Fo_{65}) in agreement with Baron *et al.* (2019), who showed that olivine reaction solutions were oxidising, hindering siderite formation. These results seem in disagreement with the iron-rich carbonate minerals observed in the nakhlite Martian meteorites (Nakhla, Lafayette, and Governador Valadares). However, they are inferred to have formed through high temperature hydrothermal subsurface processes induced by an impact event (Bridges and Schwenzer, 2012), contrasting with our experimental conditions (*i.e.* water equilibrated with a $pCO_2 = 1$ bar atmosphere, T = 45 °C). Moreover, the lower carbonation observed on the Fo_{65} compared to the Fo_{92} sample (Fig. 2) suggests that the Fe enrichment in martian olivine limits the quantity of carbonate but does not prevent its formation, in agreement with the results of Brown *et al.* (2020) who identify $Fo_{40\text{-}66}$ in the olivine-carbonate lithology of Nili Fossae region. This effect could be due to the development of an Fe-rich silica layer on the olivine surface that limits the carbonatation reaction (Oelkers *et al.*, 2018). Interestingly, in Kissick *et al.* (2021), no carbonates were detected from aqueous alteration of fayalite-forsterite mixtures, but this could be due to the FTIR detection limit. We do not identify either a carbonate signal when analysing the whole fraction of the sample with this technique.

An important question is why carbonates do not form in the crustal simulant samples. As noted by Baron *et al.* (2019), our experiments demonstrate that the mineralogy of the reactants significantly influences solution properties, particularly pH, subsequent reaction pathways, and the formation of secondary products. In a dense CO_2 atmosphere on early Mars (*i.e.* $pCO_2 =$ 1 bar), carbonate minerals are not stable at pH < 6.2 (Bullock and Moore, 2007) and the simulant samples yield solutions with pH values below this threshold (Fig. 2); the pH values of the simulant solutions are intermediate between those of pure olivine and pure feldspar samples. In our experiments, dissolution-precipitation reactions are likely coupled, and both martian simulants contain high percentages of feldspars that generally form Al-OH-rich secondary minerals (*e.g.*, amorphous Al-OH precursors, gibbsite or kaolinite) as alteration products (Zhu and Lu, 2009). The insoluble nature of the Al^{3+} under weathering conditions favours precipitation of such phases and therefore the production of H^+ by the hydrolysis of this cation (*e.g.*, $Al^{3+} + 3H_2O = Al(OH)_{3(s)} + 3H^+$). As we do not identify Al^{3+} in simulant solutions (Fig. S-7), we hypothesise that the incorporation of OH in these secondary products helps to hold the pH at slightly acidic values. Comparing the fluid chemistry of forsterite and simulant solutions (Fig. S-7) is evident that forsterite solutions hold the highest Mg^{2+} concentration from the incongruent dissolution of forsterite, favouring the formation of Mg-carbonates.

These findings suggest that the formation of carbonates by surface weathering on early Mars depends on the host rock composition, as suggested by Kissick *et al.* (2021). Accordingly, surface carbonate deposits might only have formed from olivine-rich rock (*i.e.* olivine > 20 wt. %), like in Nile Fossae region, but not from more felsic rocks. Regardless, this scenario does not preclude the formation of carbonates by migration of meteoric water and/or diffusion which would induce a pH increase with depth, groundwater circulation, or hydrothermal processes. Indeed, Thorpe *et al.* (2022) recently identified Fe-rich carbonate in Glen Torridon (Gale Crater) and inferred that it likely formed in a subsurface mixing zone between lacustrine water and deep groundwater.

Geochemical models for basalt dissolution under a CO_2-rich early Mars atmosphere generally predict more abundant carbonate formation than observed on the martian surface. However, these models usually assume olivine-rich basalts as starting protoliths (*i.e.* olivine > 20 wt. %) and equilibrium conditions. Consequently, they do not address kinetic barrier effects (Kissick *et al.*, 2021; Scheller *et al.*, 2021), which may result in an overestimation of the carbonate abundance (see geochemical modelling and carbonates in SI).

Carbonate occurrences detected on Mars are commonly associated with olivine-bearing lithologies (olivine > 20 % in volume) (Wray *et al.*, 2016), consistent with our experimental results. The Comanche outcrops in the Columbia Hills (Gusev Crater) contain a mineral assemblage of olivine and carbonates. These carbonates, of inferred Noachian age, are abundant (16 to 34 wt. %) and intimately associated with olivine (Fo_{68}) and amorphous silicate (Morris *et al.*, 2010). Orbital reflectance spectra of the Capri Chasma region also show phyllosilicates, carbonates, and a host rock potentially rich in olivine (Jain and Chauhan, 2015), like the carbonate-olivine association observed at Nili Fossae (Ehlmann *et al.*, 2009). In Jezero Crater, carbonates detected from orbit are associated with olivine-bearing rocks and mapped as the same geological unit identified across Nili Fossae (Mandon *et al.*, 2020). These alteration units share similarities with the mineralogical associations described in the oldest

carbonates identified in ALH 84001, likely formed by a low temperature weathering fluid equilibrated with CO_2 atmosphere (Halevy *et al.*, 2011).

Recent results show that the ancient Mars crust was more alkali-rich and felsic than previously thought (Sautter *et al.*, 2016), as indicated by the abundance of felsic igneous rocks (trachytic, alkali feldspar-rich) found in Gale Crater as float and pebbles sourced from Noachian age crust around the crater (Mangold *et al.*, 2016). Likewise, the ancient meteorite breccia NWA 7034 (and pairs) is rich in feldspars and lacks primary olivine (Hewins *et al.*, 2017). Regarding the olivine distribution through Mars, olivine-rich regions such as Nili Fossae (*i.e.* olivine > 20 wt. %) are rare in Noachian highlands (*e.g.*, Ody *et al.*, 2013). Our results show that a more felsic and alkali-rich crustal composition does not produce carbonates by weathering under early Mars-like conditions, *i.e.*, $pCO_2 = 1$ bar, moderate temperature. Our results are likewise consistent with the limited occurrence of carbonates (<3.2 wt. %) detected by CheMin in the Glen Torridon area of Gale Crater (Thorpe *et al.*, 2022) and the absence of carbonates in other crater locations (Bristow *et al.*, 2017), despite significant diagenetic alteration in the mudstones (*i.e.* 20 to 30 wt. % of phyllosilicates). However, the sedimentary record in Gale reveals a rich spectrum of alteration stages, which may encompass processes such as the formation-dissolution of pre-existing carbonates and the later formation of clay minerals, as observed in Nakhlites. Our results also help to illustrate why martian carbonates did not form abundant surface deposits, thus, serving as a limited storage for atmospheric CO_2 (Edwards and Ehlmann, 2015). Considering that there have been no detections of substantial CO_2 reservoirs at Mars' surface, MAVEN observations propose that gas loss to space may have driven Martian climate change (Jakosky *et al.*, 2018).

The weathering experiments presented here suggest that (1) Fo_{65} and Fo_{92} samples induce the formation of Mg carbonate (no evidence of siderite is here detected), and (2) the inhibiting effect of a more felsic composition in the early Mars crust could have on carbonate formation. As a corollary, we suggest that the sparse distribution of surface carbonates under a warmer and thicker CO_2 atmosphere can be associated with the compositional diversity of the magmatic rocks in the ancient martian crust. Therefore, their scarcity does not have to be evidence of a cold and dried early Mars.

Acknowledgements

We thank reviewers Mike Thorpe, Allan Treiman and one anonymous reviewer whose suggestions helped improve and clarify this manuscript. We thank Erwan Le Menn for his assistance during the experiment set up. This research was supported by the project "Mars-Prime" (ANR-16-CE31-0012) from the Agence Nationale de la Recherche. CG-L was supported for the Postdoctoral fellowship ED481B-2019-068 (Xunta de Galicia) and by the project PID2020-119412RJ-I00 from MICINN Spain.

Editor: Francis McCubbin

Additional Information

Supplementary Information accompanies this letter at https://www.geochemicalperspectivesletters.org/article2403.

Cite this letter as: Gil-Lozano, C., Baron, F., Gaudin, A., Lorand, J.-P., Fernandez, V., Hamon, J., Mangold, N. (2024) The key role of bedrock composition in the formation of carbonates on Mars. *Geochem. Persp. Let.* 28, 54–59. https://doi.org/10.7185/geochemlet.2403

References

Baron, F., Gaudin, A., Lorand, J.-P., Mangold, N. (2019) New Constraints on Early Mars Weathering Conditions From an Experimental Approach on Crust Simulants. *Journal of Geophysical Research: Planets* 124, 1783–1801. https://doi.org/10.1029/2019JE005920

Boynton, W.V., Ming, D.W., Kounaves, S.P., Young, S.M.M., Arvidson, R.E., Hecht, M.H., Hoffman, J., Niles, P.B., Hamara, D.K., Quinn, R.C., Smith, P.H., Sutter, B., Catling, D.C., Morris, R.V. (2009) Evidence for Calcium Carbonate at the Mars Phoenix Landing Site. *Science* 325, 61–64. https://doi.org/10.1126/science.1172768

Bridges, J.C., Schwenzer, S.P. (2012) The nakhlite hydrothermal brine on Mars. *Earth and Planetary Science Letters* 359–360, 117–123. https://doi.org/10.1016/j.epsl.2012.09.044

Bridges, J.C., Hicks, L.J., Treiman, A.H. (2019) Chapter 5 - Carbonates on Mars. In: Filiberto, J., Schwenzer, S.P. (Eds.) *Volatiles in the Martian Crust*. Elsevier, Amsterdam (Netherlands), Oxford (UK), Cambridge (USA), 89–118. https://doi.org/10.1016/B978-0-12-804191-8.00005-2

Bristow, T.F., Haberle, R.M., Blake, D.F., Des Marais, D.J., Eigenbrode, J.L., Fairén, A.G., Grotzinger, J.P., Stack, K.M., Mischna, M.A., Rampe, E.B., Siebach, K.L., Sutter, B., Vaniman, D.T., Vasavada, A.R. (2017) Low Hesperian PCO_2 constrained from in situ mineralogical analysis at Gale Crater, Mars. *Proceedings of the National Academy of Sciences* 114, 2166–2170. https://doi.org/10.1073/pnas.1616649114

Brown, A.J., Viviano, C.E., Goudge, T.A. (2020) Olivine-Carbonate Mineralogy of the Jezero Crater Region. *Journal of Geophysical Research: Planets* 125, e2019JE006011. https://doi.org/10.1029/2019JE006011

Bullock, M.A., Moore, J.M. (2007) Atmospheric conditions on early Mars and the missing layered carbonates. *Geophysical Research Letters* 34, L19201. https://doi.org/10.1029/2007GL030688

Carter, J., Riu, L., Poulet, F., Bibring, J.-P., Langevin, Y., Gondet, B. (2023) A Mars orbital catalog of aqueous alteration signatures (MOCAAS). *Icarus* 389, 115164. https://doi.org/10.1016/j.icarus.2022.115164

Dehouck, E., Gaudin, A., Mangold, N., Lajaunie, L., Dauzères, A., Grauby, O., Le Menn, E. (2014) Weathering of olivine under CO_2 atmosphere: A martian perspective. *Geochimica et Cosmochimica Acta* 135, 170–189. https://doi.org/10.1016/j.gca.2014.03.032

Edwards, C.S., Ehlmann, B.L. (2015) Carbon sequestration on Mars. *Geology* 43, 863–866. https://doi.org/10.1130/G36983.1

Ehlmann, B.L., Mustard, J.F., Swayze, G.A., Clark, R.N., Bishop, J.L., Poulet, F., Des Marais, D.J., Roach, L.H., Milliken, R.E., Wray, J.J., Barnouin-Jha, O., Murchie, S.L. (2009) Identification of hydrated silicate minerals on Mars using MRO-CRISM: Geologic context near Nili Fossae and implications for aqueous alteration. *Journal of Geophysical Research: Planets* 114, E00D08. https://doi.org/10.1029/2009JE003339

Gaudin, A., Dehouck, E., Grauby, O., Mangold, N. (2018) Formation of clay minerals on Mars: Insights from long-term experimental weathering of olivine. *Icarus* 311, 210–223. https://doi.org/10.1016/j.icarus.2018.01.029

Halevy, I., Fischer, W.W., Eiler, J.M. (2011) Carbonates in the Martian meteorite Allan Hills 84001 formed at 18 ± 4 °C in a near-surface aqueous environment. *Proceedings of the National Academy of Sciences* 108, 16895–16899. https://doi.org/10.1073/pnas.1109444108

Hewins, R.H., Zanda, B., Humayun, M., Nemchin, A., Lorand, J.-P., Pont, S., Deldicque, D., Bellucci, J.J., Beck, P., Leroux, H., Marinova, M., Remusat, L., Göpel, C., Lewin, E., Grange, M., Kennedy, A., Whitehouse, M.J. (2017) Regolith breccia Northwest Africa 7533: Mineralogy and petrology with implications for early Mars. *Meteoritics & Planetary Science* 52, 89–124. https://doi.org/10.1111/maps.12740

Horgan, B.H.N., Anderson, R.B., Dromart, G., Amador, E.S., Rice, M.S. (2020) The mineral diversity of Jezero crater: Evidence for possible lacustrine

carbonates on Mars. *Icarus* 339, 113526. https://doi.org/10.1016/j.icarus.2019.113526

Jain, N., Chauhan, P. (2015) Study of phyllosilicates and carbonates from the Capri Chasma region of Valles Marineris on Mars based on Mars Reconnaissance Orbiter-Compact Reconnaissance Imaging Spectrometer for Mars (MRO-CRISM) observations. *Icarus* 250, 7–17. https://doi.org/10.1016/j.icarus.2014.11.018

Jakosky, B.M., Brain, D., Chaffin, M., Curry, S., Deighan, J., Grebowsky, J., Halekas, J., Leblanc, F., Lillis, R., Luhmann, J.G., Andersson, L., Andre, N., Andrews, D., Baird, D., Baker, D., Bell, J., Benna, M., Bhattacharyya, D., Bougher, S., Bowers, C., Chamberlin, P., Chaufray, J.Y., Clarke, J., Collinson, G., Combi, M., Connerney, J., Connour, K., Correira, J., Crabb, K., Crary, F., Cravens, T., Crismani, M., Delory, G., Dewey, R., DiBraccio, G., Dong, C., Dong, Y., Dunn, P., Egan, H., Elrod, M., England, S., Eparvier, F., Ergun, R., Eriksson, A., Esman, T., Espley, J., Evans, S., Fallows, K., Fang, X., Fillingim, M., Flynn, C., Fogle, A., Fowler, C., Fox, J., Fujimoto, M., Garnier, P., Girazian, Z., Groeller, H., Gruesbeck, J., Hamil, O., Hanley, K.G., Hara, T., Harada, Y., Hermann, J., Holmberg, M., Holsclaw, G., Houston, S., Inui, S., Jain, S., Jolitz, R., Kotova, A., Kuroda, T., Larson, D., Lee, Y., Lee, C., Lefevre, F., Lentz, C., Lo, D., Lugo, R., Ma, Y.J., Mahaffy, P., Marquette, M.L., Matsumoto, Y., Mayyasi, M., Mazelle, C., McClintock, W., McFadden, J., Medvedev, A., Mendillo, M., Meziane, K., Milby, Z., Mitchell, D., Modolo, R., Montmessin, F., Nagy, A., Nakagawa, H., Narvaez, C., Olsen, K., Pawlowski, D., Peterson, W., *et al.* (2018) Loss of the Martian atmosphere to space: Present-day loss rates determined from MAVEN observations and integrated loss through time. *Icarus* 315, 146–157. https://doi.org/10.1016/j.icarus.2018.05.030

Kissick, L.E., Mather, T.A., Tosca, N.J. (2021) Unravelling surface and subsurface carbon sinks within the early Martian crust. *Earth and Planetary Science Letters* 557, 116663. https://doi.org/10.1016/j.epsl.2020.116663

Mandon, L., Quantin-Nataf, C., Thollot, P., Mangold, N., Lozac'h, L., Dromart, G., Beck, P., Dehouck, E., Breton, S., Millot, C., Volat, M. (2020) Refining the age, emplacement and alteration scenarios of the olivine-rich unit in the Nili Fossae region, Mars. *Icarus* 336, 113436. https://doi.org/10.1016/j.icarus.2019.113436

Mangold, N., Poulet, F., Mustard, J.F., Bibring, J.-P., Gondet, B., Langevin, Y., Ansan, V., Masson, P., Fassett, C., Head III, J.W., Hoffmann, H., Neukum, G. (2007) Mineralogy of the Nili Fossae region with OMEGA/Mars Express data: 2. Aqueous alteration of the crust. *Journal of Geophysical Research: Planets* 112, E08S04. https://doi.org/10.1029/2006JE002835

Mangold, N., Thompson, L.M., Forni, O., Williams, A.J., Fabre, C., Le Deit, L., Wiens, R.C., Williams, R., Anderson, R.B., Blaney, D.L., Calef, F., Cousin, A., Clegg, S.M., Dromart, G., Dietrich, W.E., Edgett, K.S., Fisk, M.R., Gasnault, O., Gellert, R., Grotzinger, J.P., Kah, L., Le Mouélic, S., McLennan, S.M., Maurice, S., Meslin, P.-Y., Newsom, H.E., Palucis, M.C., Rapin, W., Sautter, V., Siebach, K.L., Stack, K., Sumner, D., Yingst, A. (2016) Composition of conglomerates analyzed by the Curiosity rover: Implications for Gale Crater crust and sediment sources. *Journal of Geophysical Research: Planets* 121, 353–387. https://doi.org/10.1002/2015JE004977

McSween, H.Y., Wyatt, M.B., Gellert, R., Bell III, J.F., Morris, R.V., Herkenhoff, K.E., Crumpler, L.S., Milam, K.A., Stockstill, K.R., Tornabene, L.L., Arvidson, R.E., Bartlett, P., Blaney, D., Cabrol, N.A., Christensen, P.R., Clark, B.C., Crisp, J.A., Des Marais, D.J., Economou, T., Farmer, J.D., Farrand, W., Ghosh, A., Golombek, M., Gorevan, S., Greeley, R., Hamilton, V.E., Johnson, J.R., Joliff, B.L., Klingelhöfer, G., Knudson, A.T., McLennan, S., Ming, D., Moersch, J.E., Rieder, R., Ruff, S.W., Schröder, C., de Souza Jr., P.A., Squyres, S.W., Wänke, H., Wang, A., Yen, A., Zipfel, J. (2006) Characterization and petrologic interpretation of olivine-rich basalts at Gusev Crater, Mars. *Journal of Geophysical Research: Planets* 111, E02S10. https://doi.org/10.1029/2005JE002477

Morris, R.V., Ruff, S.W., Gellert, R., Ming, D.W., Arvidson, R.E., Clark, B.C., Golden, D.C., Siebach, K., Klingelhöfer, G., Schröder, C., Fleischer, I., Yen, A.S., Squyres, S.W. (2010) Identification of Carbonate-Rich Outcrops on Mars by the Spirit Rover. *Science* 329, 421–424. https://doi.org/10.1126/science.1189667

Ody, A., Poulet, F., Bibring, J.-P., Loizeau, D., Carter, J., Gondet, B., Langevin, Y. (2013) Global investigation of olivine on Mars: Insights into crust and mantle compositions. *Journal of Geophysical Research: Planets* 118, 234–262. https://doi.org/10.1029/2012JE004149

Oelkers, E., Declercq, J., Saldi, G., Gislason, S. (2018) Olivine dissolution rates: A critical review. *Chemical Geology* 500, 1–19. https://doi.org/10.1016/j.chemgeo.2018.10.008

Sautter, V., Toplis, M.J., Beck, P., Mangold, N., Wiens, R., Pinet, P., Cousin, A., Maurice, S., LeDeit, L., Hewins, R., Gasnault, O., Quantin, C., Forni, O., Newsom, H., Meslin, P.-Y., Wray, J., Bridges, N., Payré, V., Rapin, W., Le Mouélic, S. (2016) Magmatic complexity on early Mars as seen through a combination of orbital, in-situ and meteorite data. *Lithos* 254–255, 36–52. https://doi.org/10.1016/j.lithos.2016.02.023

Scheller, E.L., Swindle, C., Grotzinger, J., Barnhart, H., Bhattacharjee, S., Ehlmann, B.L., Farley, K., Fischer, W.W., Greenberger, R., Ingalls, M., Martin, P.E., Osorio-Rodriguez, D., Smith, B.P. (2021) Formation of Magnesium Carbonates on Earth and Implications for Mars. *Journal of Geophysical Research: Planets* 126, e2021JE006828. https://doi.org/10.1029/2021JE006828

Snæbjörnsdóttir, S.Ó., Sigfússon, B., Marieni, C., Goldberg, D., Gislason, S.R., Oelkers, E.H. (2020) Carbon dioxide storage through mineral carbonation. *Nature Reviews Earth & Environment* 1, 90–102. https://doi.org/10.1038/s43017-019-0011-8

Thorpe, M.T., Bristow, T.F., Rampe, E.B., Tosca, N.J., Grotzinger, J.P., Bennett, K.A., Achilles, C.N., Blake, D.F., Chipera, S.J., Downs, G., Downs, R.T., Morrison, S.M., Tu, V., Castle, N., Craig, P., Marais, D.J.D., Hazen, R.M., Ming, D.W., Morris, R.V., Treiman, A.H., Vaniman, D.T., Yen, A.S., Vasavada, A.R., Dehouck, E., Bridges, J.C., Berger, J., McAdam, A., Peretyazhko, T., Siebach, K.L., Bryk, A.B., Fox, V.K., Fedo, C.M. (2022) Mars Science Laboratory CheMin Data From the Glen Torridon Region and the Significance of Lake-Groundwater Interactions in Interpreting Mineralogy and Sedimentary History. *Journal of Geophysical Research: Planets* 127, e2021JE007099. https://doi.org/10.1029/2021JE007099

Wray, J.J., Murchie, S.L., Bishop, J.L., Ehlmann, B.L., Milliken, R.E., Wilhelm, M.B., Seelos, K.D., Chojnacki, M. (2016) Orbital evidence for more widespread carbonate-bearing rocks on Mars. *Journal of Geophysical Research: Planets* 121, 652–677. https://doi.org/10.1002/2015JE004972

Zhu, C., Lu, P. (2009) Alkali feldspar dissolution and secondary mineral precipitation in batch systems: 3. Saturation states of product minerals and reaction paths. *Geochimica et Cosmochimica Acta* 73, 3171–3200. https://doi.org/10.1016/j.gca.2009.03.015

Geochemical Perspectives Letters

The key role of bedrock composition in the formation of carbonates on Mars

C. Gil-Lozano, F. Baron, A. Gaudin, J.-P. Lorand, V. Fernandez, J. Hamon, N. Mangold

Supplementary Information

The Supplementary Information includes:

- Materials and Methods
- Table S-1
- Figures S-1 to S-8
- Geochemical Modelling and Carbonates
- Supplementary Information References

Materials and methods

Starting materials and experimental set-up. As starting minerals we chose a list of individual minerals, namely forsterite – magnesium and iron-rich-, clinopyroxene, plagioclase, and potassium feldspar, as well as two prepared martian crust simulants constrained by the early Mars crust composition inferred by the conglomerate analysed in the Gale crater (Mangold *et al.*, 2016) and the Martian regolith breccia NWA 7533 and NWA 7034 (Agee *et al.*, 2013; Humayun *et al.*, 2013; Hewins *et al.*, 2017) (Table 1). These martian crust simulants were built by a mixture of individual minerals. This procedure allowed us to increase the dissolution rate of silicate minerals under low temperature conditions. The bulk chemical composition of Mars simulants samples was estimated according to the proportion of the minerals (wt. % in Table 1). Both Mars crust simulants present a high proportion of K-feldspars to balance the low Na-content of plagioclase and fit the alkali-rich composition of martian regolith breccias. Specifically, in a total alkali-silica (TAS) diagram (Le Bas *et al.*, 1986) the chemical composition of simulant containing Fo_{65}-olivine (Sim-O) is consistent with basaltic andesite, whereas the simulant containing magnetite but lacking olivine (Sim-M), with high Fe content fits better with a basaltic composition. Each mineral was crushed, sieved (Ø < 63 µm) and settled in ethanol to remove the fine fraction (Ø < 2 µm).

Aqueous alteration experiments reproducing martian weathering under a thick CO_2 atmosphere were performed under a controlled anoxic CO_2 atmosphere (*i.e.* Mbraun-LABstar glovebox with a constant pCO_2 = 1 bar, Air Liquide® Alphagaz CO_2) for 6 months (Baron *et al.*, 2019) (Fig. S-1). The O_2 concentration was continuously monitored with an oxygen analyser (MB-OX-EC-PLC, over the 1- to 1000 ppm range) and kept below pO_2 < 0.5 ppm by a gas purification unit. The samples were placed into batch Savillex™ PFA reactors (90 mL– references 100-0090-01 for the reactor and 600-053-20 for the closure) (containing 1.8 g of starting material and 18 mL of ultrapure water, 18 MΩ cm) and allowed

to react in closed conditions at a relatively low water-to-rock ratio (W/R ~10 by weight). Milli-Q® ultrapure water (18 MΩ cm) was previously degassed three times under vacuum for 3 hours each time and then equilibrated under continuous stirring for 2 days with 1 atm of CO_2. The batch reactors were kept under continuous stirring (50 rpm using an orbital agitator) and at 45 °C (thermostatic hot plate) to increase the reaction rate. Initial pH values of anoxic ultrapure water were measured after 2 days of stirring conditions inside the glovebox to ensure equilibrium with pCO_2 = 1 bar atmosphere (pH_0 = 3.6). The final pH values of each experimental solution were measured at the end of the experiments in contact with minerals at 25 °C. The pH values were then estimated at 45 °C for each experimental solution from thermodynamic calculations. The calculations were performed using the PHREEQC® software (Parkhurst and Apello, 2014) associated with the Thermoddem database (http://thermoddem.brgm.fr/), further details concerning the sample preparation and experimental design can be found in Baron *et al.* (2019).

After 6 months of reaction, the samples were filtered (< 0.2 µm) and dried inside the glovebox to separate the solid product from the solutions. The previous work of Baron *et al.* (2019) analysed the physicochemical parameters of the experimental solutions. Here, we analyse the carbonate in the solid products, but some information about fluid chemistry that helps us to discuss the results can be found in Figures S-7 and S-8.

Analytical techniques. The initial and altered samples were analysed with X-ray photoelectron spectroscopy (XPS), Fourier transforms infrared spectroscopy (FTIR), and Field Emission Gun Scanning Electron Microscope (FEG-SEM).

XPS analyses were performed using a Kratos Axis Nova spectrometer (Institut de Matériaux de Nantes, IMN, Nantes) equipped with a monochromatic Al-Kα (hν = 1486.6 eV) with a surface analysed of 700 µm x 300 µm. The base pressure of the system was below 10^{-9} mbar. Survey spectra were acquired by using 160 eV pass energy, whereas a 40 eV pass energy was applied for the analysis of the core level spectra (C1s, Si 2p, O1s, Mg 2p, and Fe2p). With the pass energy 160 eV and 40 eV, the all-over instrument resolution on the Fermi edge is about 1.9 eV and 0.56 eV, respectively. All data were acquired using charge compensation to establish a steady-state surface potential.

Mid-Infrared spectra (MIR: 4000-400 cm^{-1}) were collected using an FTIR-Nicolet 5700 spectrometer (LPG, Nantes), using a DTGS KBr detector, and a KBr beamsplitter at 4 cm^{-1} resolution. All spectra correspond to an addition of 100 scans. The analyses were carried out on the bulk samples (*i.e.*, whole size fractions) and the finest fraction (particle size <1 µm) of the reacted samples. This fine fraction was extracted by the sedimentation method based on Stokes' law in ultrapure water (18 MΩ cm) inside the glovebox, subsequently filtered (< 0.2 µm), and allowed to dry under the controlled CO_2 atmosphere. Then, it was dispersed in a KBr matrix and measured under room conditions.

Field Emission Gun Scanning Electron Microscope (FEG-SEM) images were acquired using a JEOL JSM 7600F scanning electron microscope equipped with an Energy Dispersive Spectrometer (EDS) (IMN, Nantes).

Processing XPS data. XPS spectra were referenced to the C1s peak at 284.8 eV and analysed using CasaXPS software (version 2.3.24rev1.OR) (Fairley *et al.*, 2021). The XPS survey spectra provide information on the chemical composition of the samples (Fig. S-1), whereas C1s spectra provide the chemical composition of the carbon species. We focused on the C1s high-resolution spectra for carbonate species because the O1s orbitals are hard to deconvolve due to the presence of several oxygen-bearing species (*i.e.*, oxides, hydroxides, silicates, carbonates) and can occur within a narrow range of binding energies (Kloprogge and Wood, 2020). In the C1s spectra, all the samples present the usual contribution of ubiquitous adventitious carbon due to the physisorption of hydrocarbon layers from both the exposure to the atmosphere and the vacuum system of the instrument (Cánneva *et al.*, 2017; Kloprogge and Wood, 2020). We performed a curve fitting of the C1s high-resolution spectra to determine the amount of the carbonate component in the samples using reported literature values (Payne *et al.*, 2011; Kloprogge and Wood, 2020). The fit was performed with fixed components positions resulting in good FWHM homogeneity (Fig. 1, Fig. S-2, and Table S-1). Specifically, we used four components for the ubiquitous hydrocarbon species (Payne *et al.*, 2011): C-C/C-H (284.8 ± 0.1 eV); C-O (286.1 ± 0.1 eV); C=O (287.7 ± 0.1 eV) and O-C=O (288.7 ± 0.1eV); whereas the carbonate component position was assigned with higher deviation (289.7+/-0.4 eV) because it depends on the ionic character of the metal-carbon bond (*e.g.*, $MgCO_3$~ 290 eV and $CaCO_3$/$FeCO_3$ ~289.5 eV) (Kloprogge and Wood, 2020). We used a Voigt line Lorentzian Asymmetric (LA) function for the line shape and a U 2 Tougaard function for the background. Individual peak parameters of the fitting

can be found in Table S-1. To obtain a comprehensive overview of the total amount of the surface carbonates formed (Fig. 2), we normalised the percentages of carbonate species from the high-resolution spectra (Table S-1) to the total carbon content on the surface estimated from the survey spectra (Fig. S-1). Then, we subtracted the contribution of hydrocarbon adventitious species and the oxygen component related to them using the calculator described by Payne *et al.* (2011) and recalculated the % of the carbonate component.

Supplementary Tables

Table S-1 Individual peak parameters identified in the fitting of the C1s high-resolution spectra for iron-rich olivine (Fo_{65}-olivine), magnesium-rich olivine (Fo_{92}-olivine), clinopyroxene (cpx), potassium-feldspar (k-spar), plagioclase (PLA), simulant with olivine (Sim-O) and simulant with magnetite (Sim-M) (Fig. 1 and extended Fig. S-2)

Fo_{65}-olivine initial (residual STD=1.06)

Name	Position	FWHM	%Con.
C-C, C-H	284.8	1.5	75.2
C-O	286.2	1.5	13.8
C=O	287.8	1.5	1.5
O-C=O	288.8	1.5	7.3
CO_3	289.9	1.4	2.2

Fo_{65}-olivine reacted (CO_2 atm) (residual STD=0.80)

Name	Position	FWHM	%Con.
C-C, C-H	284.8	1.6	63.1
C-O	286.2	1.6	14.0
C=O	287.7	1.6	3.6
O-C=O	288.7	1.6	1.9
CO_3	290.1	2.0	17.4

Fo_{92}-olivine initial (residual STD= 1.15)

Name	Position	FWHM	%Con.
C-C, C-H	284.8	1.6	72.1
C-O	286.2	1.6	16.2
C=O	287.6	1.6	1.9
O-C=O	288.8	1.6	7.6
CO_3	289.9	1.6	2.2

Fo_{92}-olivine reacted (CO_2 atm) (residual STD=1.02)

Name	Position	FWHM	%Con.
C-C, C-H	284.8	1.6	64.9
C-O	286.3	1.6	15.3
C=O	287.6	1.6	3.7
O-C=O	288.6	1.6	1.7
CO_3	290.1	2.1	14.5

Cpx initial (residual STD=0.95)

Cpx reacted (CO_2 atm) (residual STD=1.34)

Name	Position	FWHM	%Con.
C-C, C-H	284.8	1.6	66.3
C-O	286.1	1.6	21.0
C=O	287.6	1.6	4.6
O-C=O	288.8	1.6	3.5
CO_3	289.7	2.0	4.6

Name	Position	FWHM	%Con.
C-C, C-H	284.8	1.6	75.4
C-O	286.2	1.6	14.6
C=O	287.6	1.6	2.1
O-C=O	288.8	1.6	5.1
CO_3	289.4	1.4	2.8

K-spar initial (residual STD=0.94)

K-spar reacted (CO_2 atm) (residual STD=1.33)

Name	Position	FWHM	%Con.
C-C, C-H	284.8	1.5	91.0
C-O	286.1	1.5	8.7
C=O	287.6	1.5	0.3
O-C=O	288.8	1.5	0.0

Name	Position	FWHM	%Con.
C-C, C-H	284.8	1.6	83.4
C-O	286.1	1.6	15.2
C=O	287.6	1.6	1.4
O-C=O	288.7	1.6	0.0

Pla initial (residual STD=1.33)

Name	Position	FWHM	%Con.
C-C, C-H	284.8	1.6	73.9
C-O	286.1	1.6	18.5
C=O	287.6	1.6	2.6
O-C=O	288.8	1.6	2.3
CO_3	289.5	1.8	2.7

Pla reacted (CO_2 atm) (residual STD=1.02)

Name	Position	FWHM	%Con.
C-C, C-H	284.8	1.5	74.3
C-O	286.1	1.5	15.8
C=O	287.6	1.5	3.2
O-C=O	288.8	1.5	2.1
CO_3	289.5	1.7	4.6

Sim-O initial (residual STD=1.55)

Name	Position	FWHM	%Con.
C-C, C-H	284.8	1.6	69.2
C-O	286.2	1.6	21.7
C=O	287.8	1.6	3.1
O-C=O	288.6	1.6	2.7
CO_3	289.4	1.8	3.3

Sim-O reacted (CO_2 atm) (residual STD=1.71)

Name	Position	FWHM	%Con.
C-C, C-H	284.8	1.6	69.0
C-O	286.2	1.6	22.2
C=O	287.8	1.6	3.4
O-C=O	288.8	1.6	0.9
CO_3	289.4	1.9	4.5

Sim-M initial (residual STD=1.34)

Name	Position	FWHM	%Con.
C-C, C-H	284.8	1.6	72.6
C-O	286.2	1.6	20.1
C=O	287.8	1.6	3.0
O-C=O	288.8	1.6	1.3
CO_3	289.4	1.8	3.1

Sim-M reacted (CO_2 atm) (residual STD=2.44)

Name	Position	FWHM	%Con.
C-C, C-H	284.8	1.6	69.9
C-O	286.2	1.6	22.1
C=O	287.8	1.6	2.9
O-C=O	288.6	1.6	0.3
CO_3	289.5	1.9	4.8

Supplementary Figures

a) b)

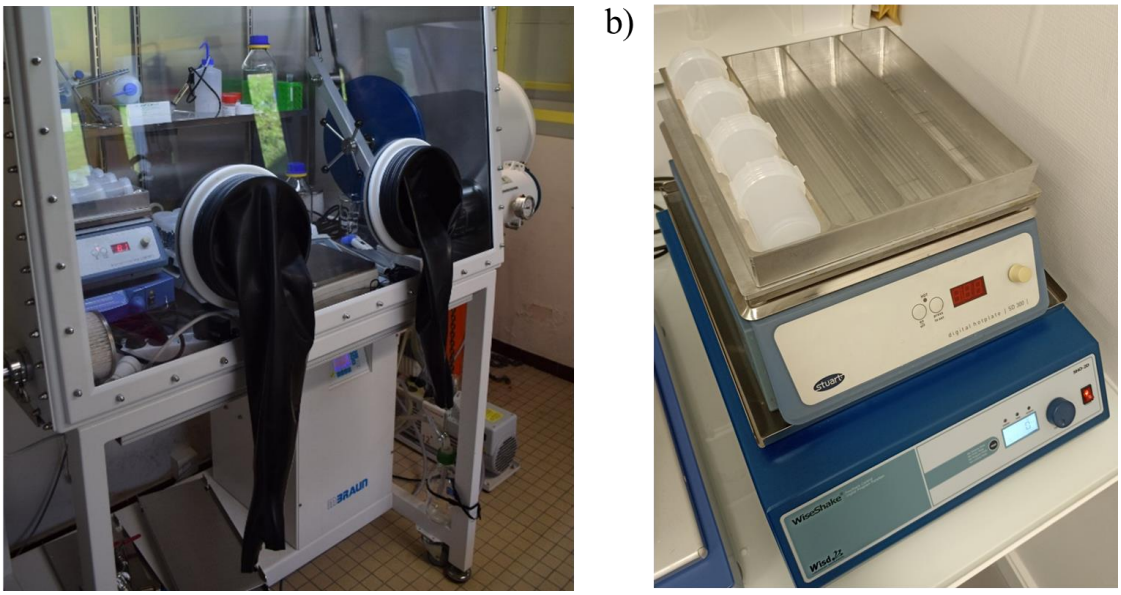

Figure S-1 **(a)** Picture of the experiment running in the glovebox. **(b)** Picture of the reactors, showing from down to top: stirring plate, hot plate and, an aluminium sample holder for the heat conductivity.

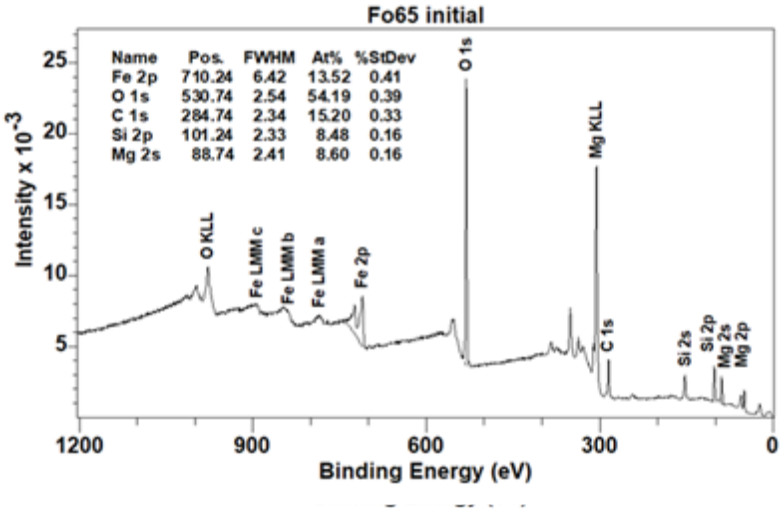
Fo65 initial
Name Pos. FWHM At% %StDev
Fe 2p 710.24 6.42 13.52 0.41
O 1s 530.74 2.54 54.19 0.39
C 1s 284.74 2.34 15.20 0.33
Si 2p 101.24 2.33 8.48 0.16
Mg 2s 88.74 2.41 8.60 0.16
Intensity x 10^-3
Binding Energy (eV)
O 1s
Mg KLL
O KLL
Fe LMM c
Fe LMM b
Fe LMM a
Fe 2p
C 1s
Si 2s
Si 2p
Mg 2s
Mg 2p

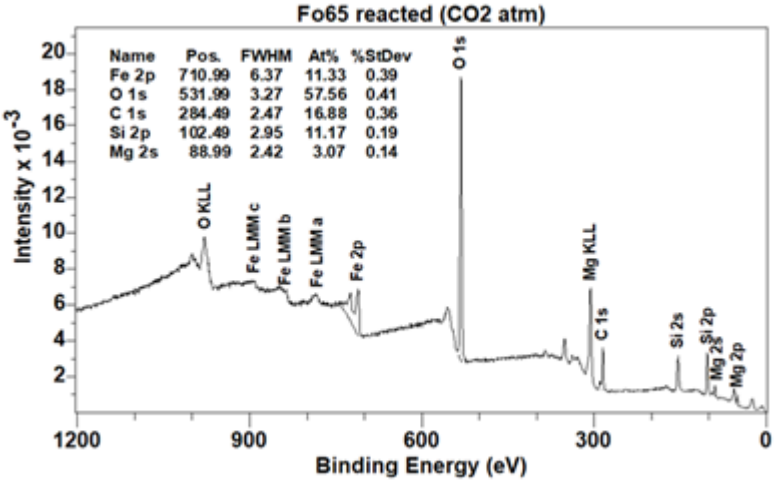
Fo65 reacted (CO2 atm)
Name Pos. FWHM At% %StDev
Fe 2p 710.99 6.37 11.33 0.39
O 1s 531.99 3.27 57.56 0.41
C 1s 284.49 2.47 16.88 0.36
Si 2p 102.49 2.95 11.17 0.19
Mg 2s 88.99 2.42 3.07 0.14
Intensity x 10^-3
Binding Energy (eV)
O 1s
O KLL
Fe LMM c
Fe LMM b
Fe LMM a
Fe 2p
Mg KLL
C 1s
Si 2s
Si 2p
Mg 2s
Mg 2p

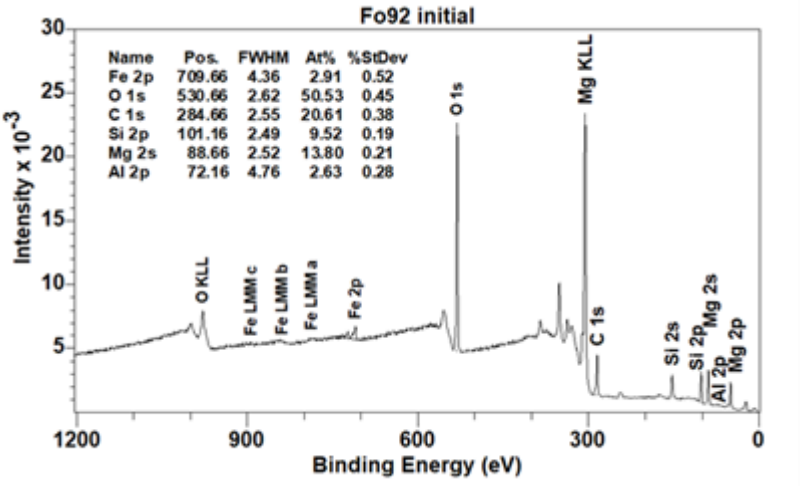
Fo92 initial
Name Pos. FWHM At% %StDev
Fe 2p 709.66 4.36 2.91 0.52
O 1s 530.66 2.62 50.53 0.45
C 1s 284.66 2.55 20.61 0.38
Si 2p 101.16 2.49 9.52 0.19
Mg 2s 88.66 2.52 13.80 0.21
Al 2p 72.16 4.76 2.63 0.28
Intensity x 10^-3
Binding Energy (eV)
O 1s
Mg KLL
O KLL
Fe LMM c
Fe LMM b
Fe LMM a
Fe 2p
C 1s
Si 2s
Si 2p
Mg 2s
Al 2p
Mg 2p

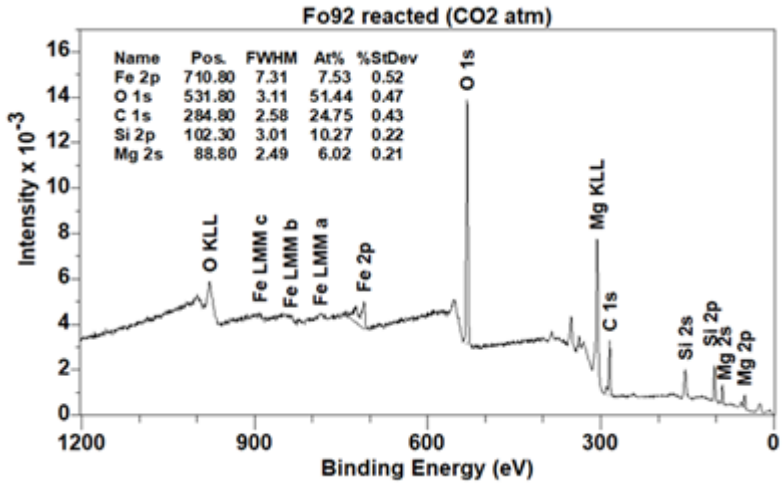
Fo92 reacted (CO2 atm)
Name Pos. FWHM At% %StDev
Fe 2p 710.80 7.31 7.53 0.52
O 1s 531.80 3.11 51.44 0.47
C 1s 284.80 2.58 24.75 0.43
Si 2p 102.30 3.01 10.27 0.22
Mg 2s 88.80 2.49 6.02 0.21
O 1s
Mg KLL
O KLL
Fe LMM c
Fe LMM b
Fe LMM a
Fe 2p
C 1s
Si 2s
Si 2p
Mg 2s
Mg 2p
Intensity x 10-3
Binding Energy (eV)

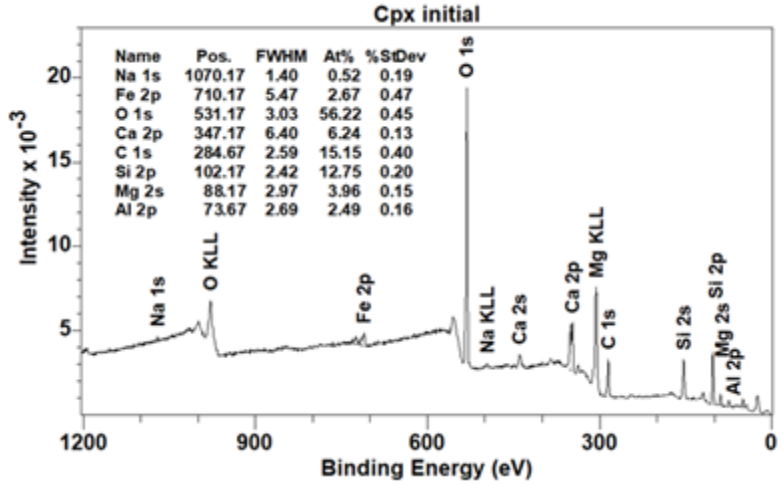
Cpx initial
Name Pos. FWHM At% %StDev
Na 1s 1070.17 1.40 0.52 0.19
Fe 2p 710.17 5.47 2.67 0.47
O 1s 531.17 3.03 56.22 0.45
Ca 2p 347.17 6.40 6.24 0.13
C 1s 284.67 2.59 15.15 0.40
Si 2p 102.17 2.42 12.75 0.20
Mg 2s 88.17 2.97 3.96 0.15
Al 2p 73.67 2.69 2.49 0.16
O 1s
Na 1s
O KLL
Fe 2p
Na KLL
Ca 2s
Ca 2p
Mg KLL
C 1s
Si 2s
Si 2p
Mg 2s
Al 2p
Intensity x 10-3
Binding Energy (eV)

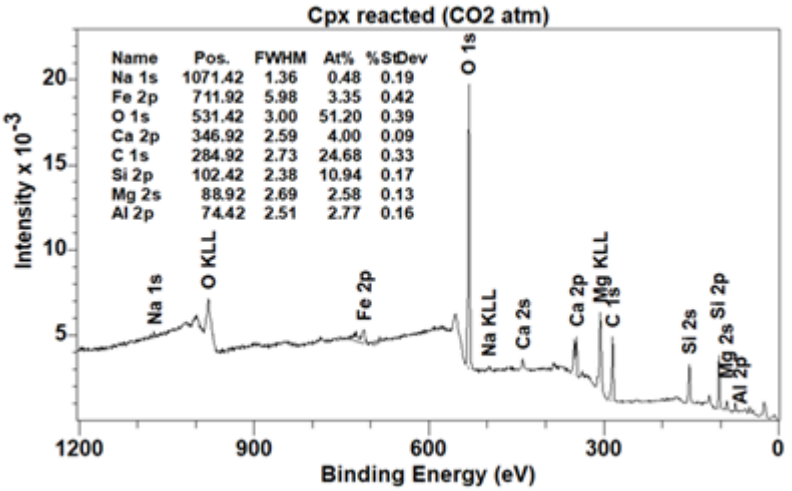
Cpx reacted (CO2 atm)
Name Pos. FWHM At% %StDev
Na 1s 1071.42 1.36 0.48 0.19
Fe 2p 711.92 5.98 3.35 0.42
O 1s 531.42 3.00 51.20 0.39
Ca 2p 346.92 2.59 4.00 0.09
C 1s 284.92 2.73 24.68 0.33
Si 2p 102.42 2.38 10.94 0.17
Mg 2s 88.92 2.69 2.58 0.13
Al 2p 74.42 2.51 2.77 0.16
O 1s
Na 1s
O KLL
Fe 2p
Na KLL
Ca 2s
Ca 2p
Mg KLL
C 1s
Si 2s
Si 2p
Mg 2s
Al 2p
Intensity x 10-3
Binding Energy (eV)

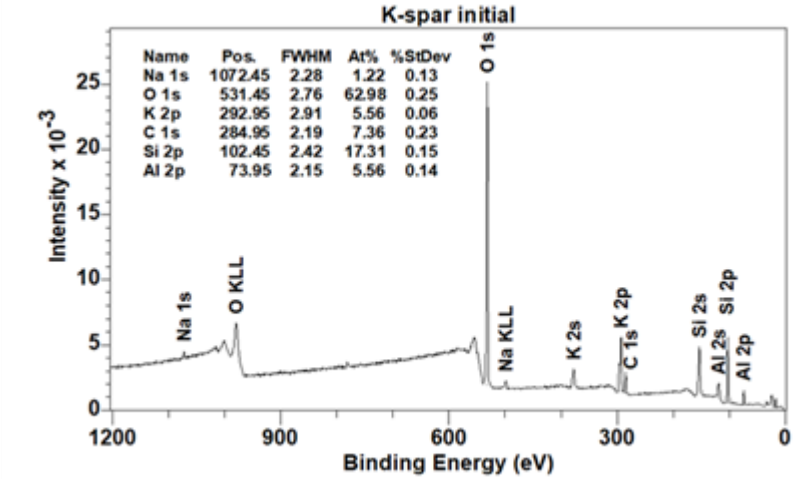
K-spar initial
Name Pos. FWHM At% %StDev
Na 1s 1072.45 2.28 1.22 0.13
O 1s 531.45 2.76 62.98 0.25
K 2p 292.95 2.91 5.56 0.06
C 1s 284.95 2.19 7.36 0.23
Si 2p 102.45 2.42 17.31 0.15
Al 2p 73.95 2.15 5.56 0.14
Intensity x 10-3
Binding Energy (eV)
O 1s
O KLL
Na 1s
Na KLL
K 2s
K 2p
C 1s
Si 2s
Al 2s
Si 2p
Al 2p

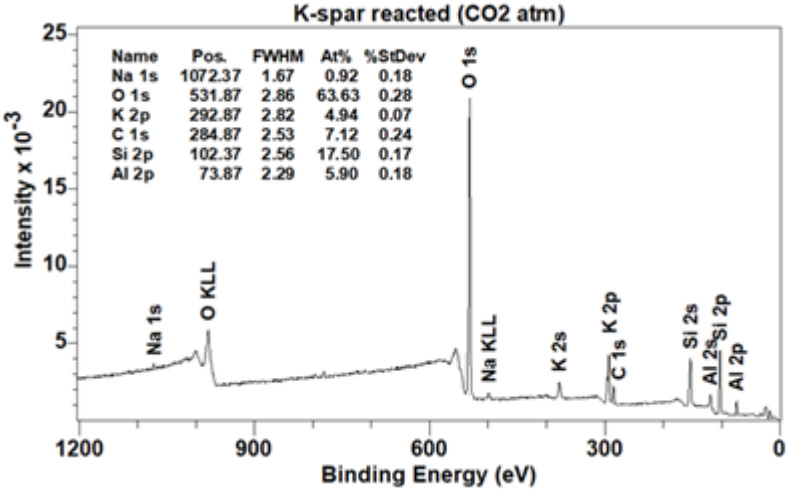
K-spar reacted (CO2 atm)
Name Pos. FWHM At% %StDev
Na 1s 1072.37 1.67 0.92 0.18
O 1s 531.87 2.86 63.63 0.28
K 2p 292.87 2.82 4.94 0.07
C 1s 284.87 2.53 7.12 0.24
Si 2p 102.37 2.56 17.50 0.17
Al 2p 73.87 2.29 5.90 0.18
Intensity x 10-3
Binding Energy (eV)
O 1s
O KLL
Na 1s
Na KLL
K 2s
K 2p
C 1s
Si 2s
Al 2s
Si 2p
Al 2p

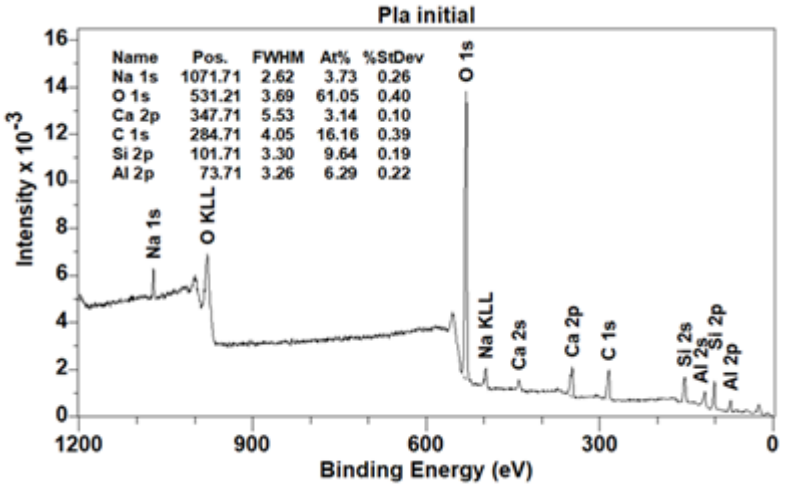
Pla initial
Name Pos. FWHM At% %StDev
Na 1s 1071.71 2.62 3.73 0.26
O 1s 531.21 3.69 61.05 0.40
Ca 2p 347.71 5.53 3.14 0.10
C 1s 284.71 4.05 16.16 0.39
Si 2p 101.71 3.30 9.64 0.19
Al 2p 73.71 3.26 6.29 0.22
Intensity x 10-3
Binding Energy (eV)
O 1s
O KLL
Na 1s
Na KLL
Ca 2s
Ca 2p
C 1s
Si 2s
Al 2s
Si 2p
Al 2p

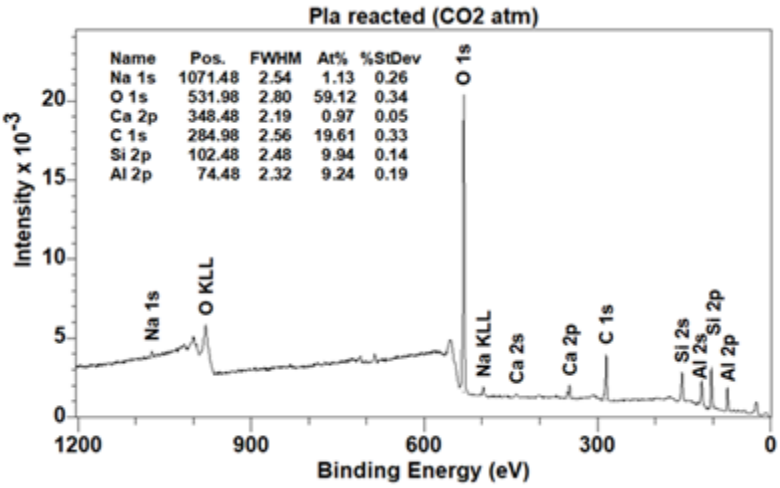
Pla reacted (CO2 atm)
Name Pos. FWHM At% %StDev
Na 1s 1071.48 2.54 1.13 0.26
O 1s 531.98 2.80 59.12 0.34
Ca 2p 348.48 2.19 0.97 0.05
C 1s 284.98 2.56 19.61 0.33
Si 2p 102.48 2.48 9.94 0.14
Al 2p 74.48 2.32 9.24 0.19
Intensity x 10^-3
Binding Energy (eV)
Na 1s
O KLL
O 1s
Na KLL
Ca 2s
Ca 2p
C 1s
Si 2s
Al 2s
Si 2p
Al 2p

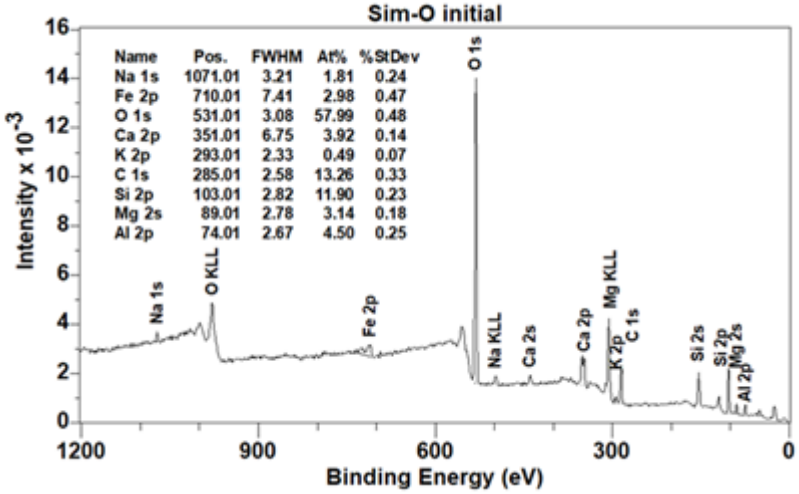
Sim-O initial
Name Pos. FWHM At% %StDev
Na 1s 1071.01 3.21 1.81 0.24
Fe 2p 710.01 7.41 2.98 0.47
O 1s 531.01 3.08 57.99 0.48
Ca 2p 351.01 6.75 3.92 0.14
K 2p 293.01 2.33 0.49 0.07
C 1s 285.01 2.58 13.26 0.33
Si 2p 103.01 2.82 11.90 0.23
Mg 2s 89.01 2.78 3.14 0.18
Al 2p 74.01 2.67 4.50 0.25
Intensity x 10^-3
Binding Energy (eV)
Na 1s
O KLL
Fe 2p
O 1s
Na KLL
Ca 2s
Ca 2p
Mg KLL
K 2p
C 1s
Si 2s
Si 2p
Mg 2s
Al 2p

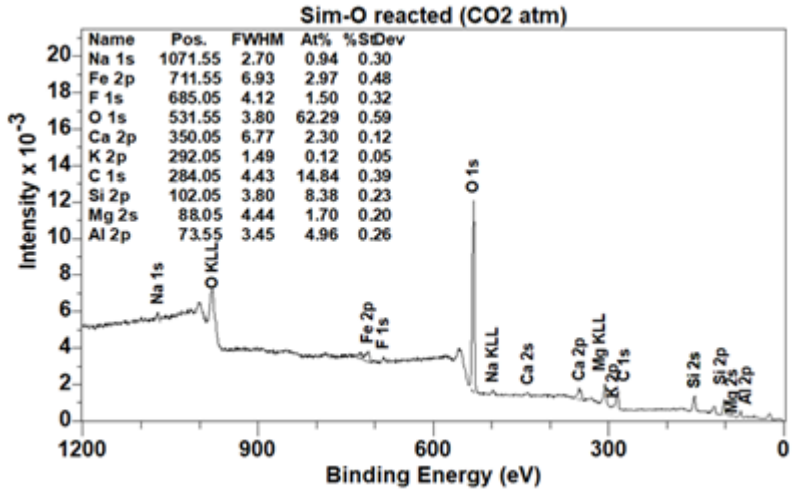
Sim-O reacted (CO2 atm)
Name Pos. FWHM At% %StDev
Na 1s 1071.55 2.70 0.94 0.30
Fe 2p 711.55 6.93 2.97 0.48
F 1s 685.05 4.12 1.50 0.32
O 1s 531.55 3.80 62.29 0.59
Ca 2p 350.05 6.77 2.30 0.12
K 2p 292.05 1.49 0.12 0.05
C 1s 284.05 4.43 14.84 0.39
Si 2p 102.05 3.80 8.38 0.23
Mg 2s 88.05 4.44 1.70 0.20
Al 2p 73.55 3.45 4.96 0.26
Intensity x 10^-3
Binding Energy (eV)
Na 1s
O KLL
Fe 2p
F 1s
O 1s
Na KLL
Ca 2s
Ca 2p
Mg KLL
K 2p
C 1s
Si 2s
Si 2p
Mg 2s
Al 2p

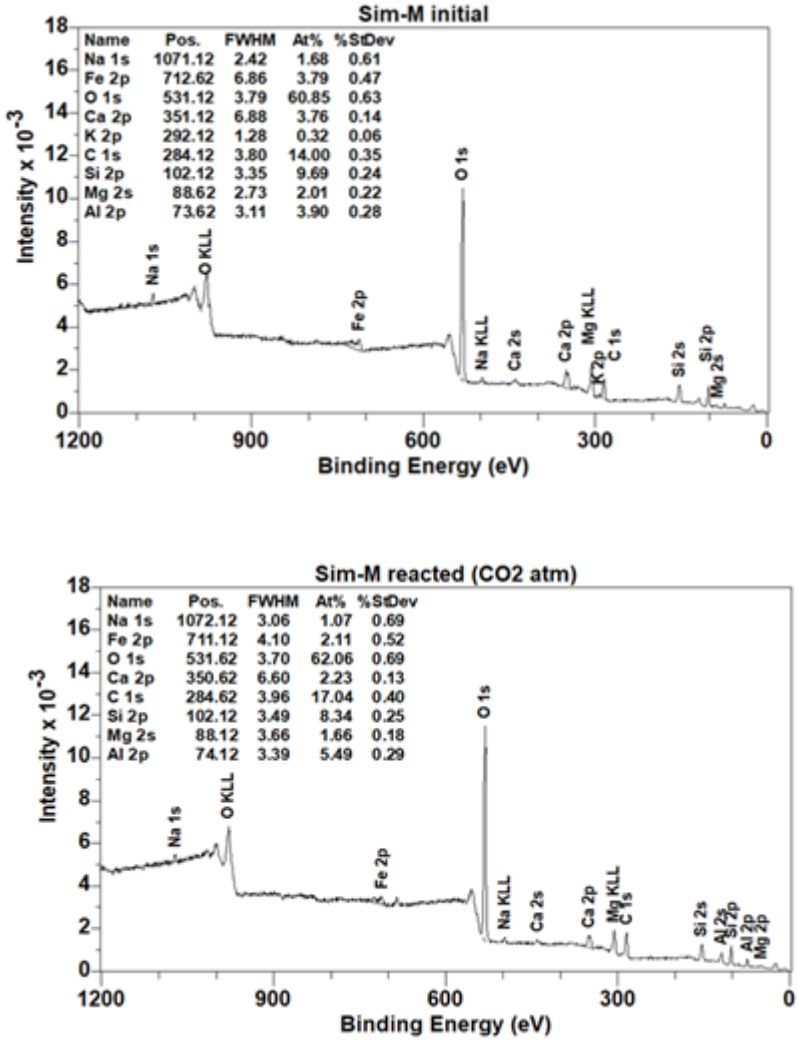

Figure S-2 Quantification of XPS survey spectra from the samples analysed in this study. From the top to the bottom, initial (before reaction) and reacted (after aqueous alteration under pCO_2): Fo_{65}-olivine (Fo_{65}); Fo_{92}-olivine (Fo_{92}); augite (Cpx); K-feldspar (K-spar); anorthite (Pla); simulant-O (Sim-O); simulant-M (Sim-M).

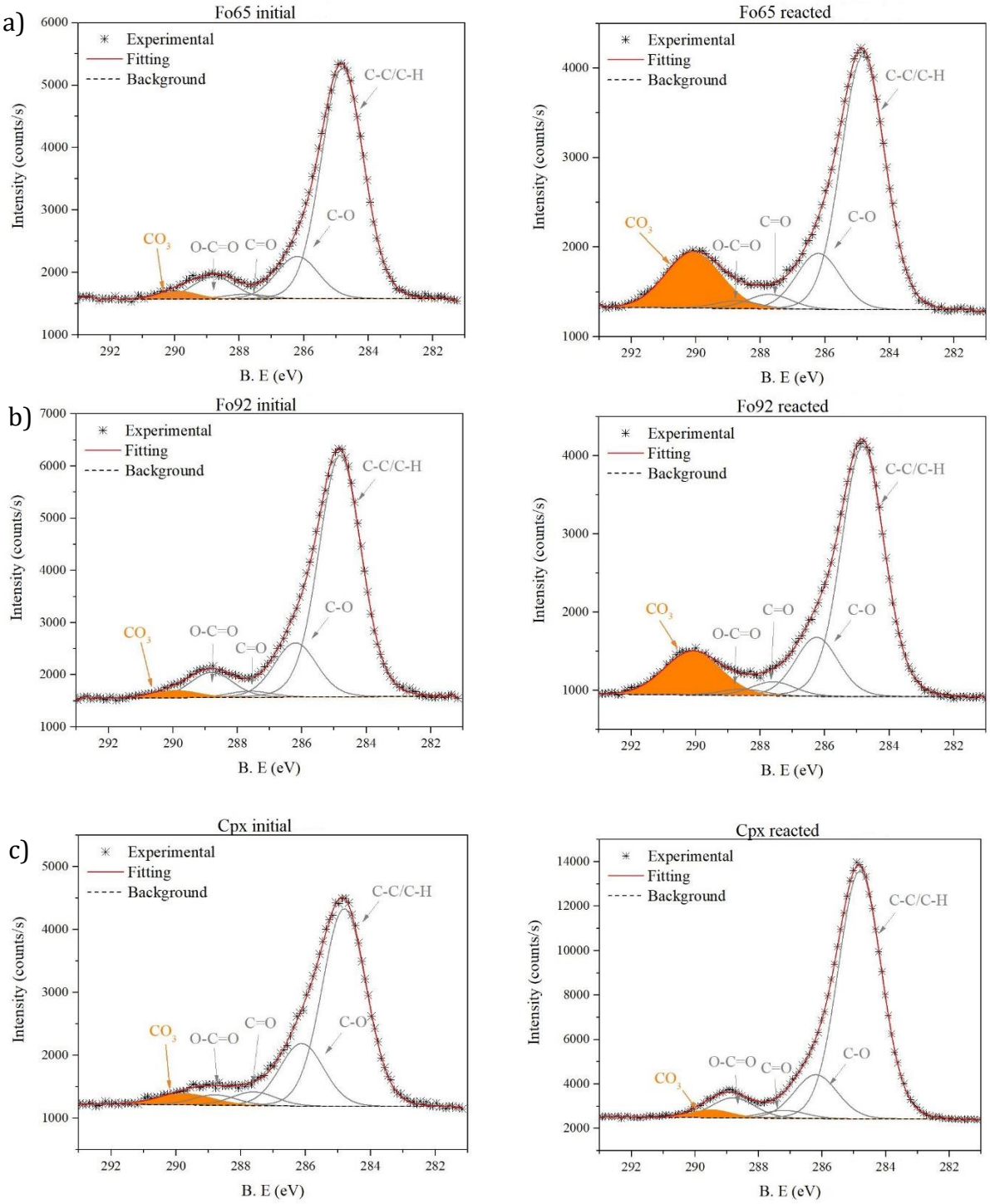
a)
Fo65 initial
Fo65 reacted
b)
Fo92 initial
Fo92 reacted
c)
Cpx initial
Cpx reacted
Experimental
Fitting
Background
C-C/C-H
C-O
C=O
O-C=O
CO3
Intensity (counts/s)
B. E (eV)

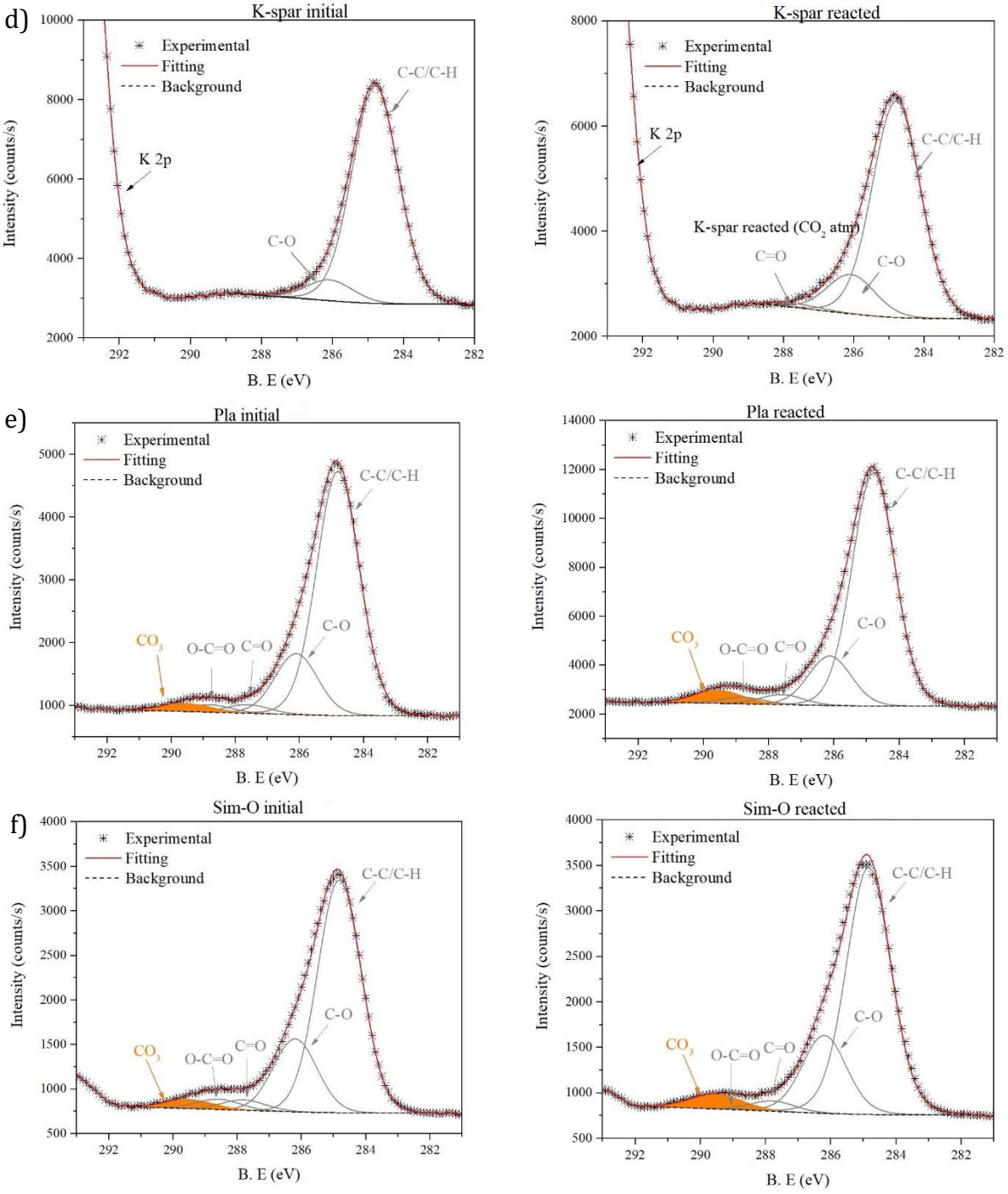
d)
K-spar initial
Experimental
Fitting
Background
K 2p
C-C/C-H
C-O
Intensity (counts/s)
B. E (eV)
K-spar reacted
K-spar reacted (CO2 atm)
C=O
e)
Pla initial
Pla reacted
CO3
O-C=O
C=O
f)
Sim-O initial
Sim-O reacted

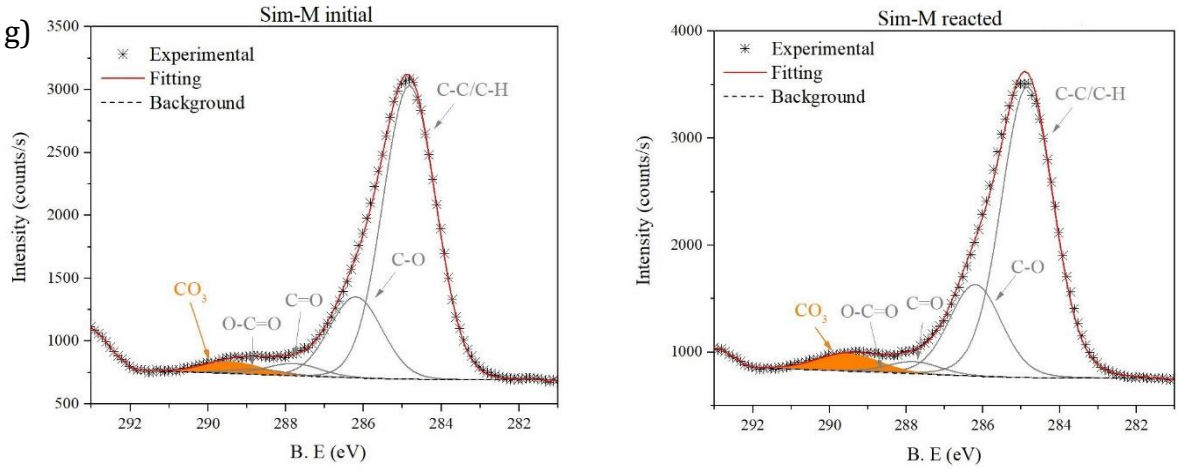

Figure S-3 Fitting model of high-resolution C1s spectra to identify adventitious carbon (grey) and carbonate species (orange). Individual peak parameters are shown in Table S.1. The left column shows the initial samples and the right the reacted samples under a CO_2 atmosphere: **(a)** Fo_{65}-olivine (Fo_{65}), **(b)** Fo_{92}-olivine (Fo_{92}), **(c)** clinopyroxene (Cpx), **(d)** potassium feldspar (K-spar), **(e)** plagioclase (Pla), **(f)** Mars crust simulant-O (Sim-O) and, **(g)** Mars crust simulant-M (Sim-M).

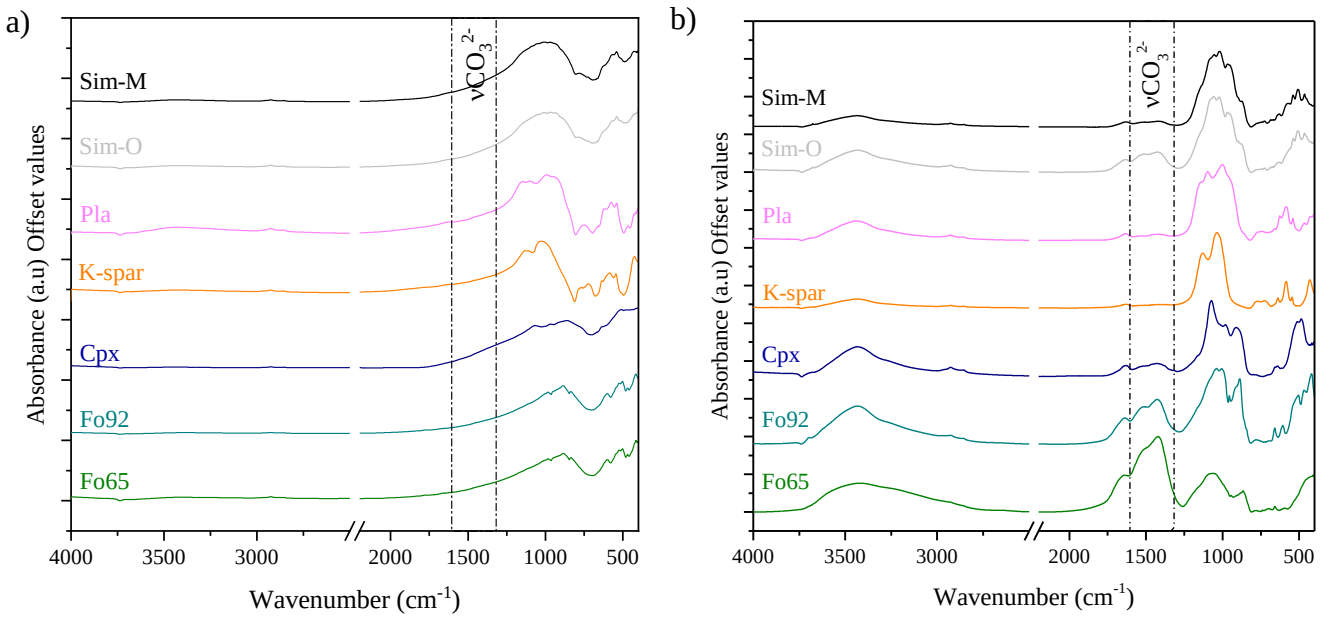

Figure S-4 Mid-IR spectra of reacted samples: **(a)** bulk samples, **(b)** size fraction <1 µm. From the bottom to the top: Fo_{65}-olivine (Fo_{65}), Fo_{92}-olivine (Fo_{92}), clinopyroxene (Cpx), K-feldspar (K-spar), plagioclase (Pla), simulant-O (Sim-O), and simulant-M (Sim-M). Dashed lines mark the region of the asymmetric stretching vibration of the carbonates group ($\nu_3(CO_3)^{2-}$) (Jones and Jackson, 1993).

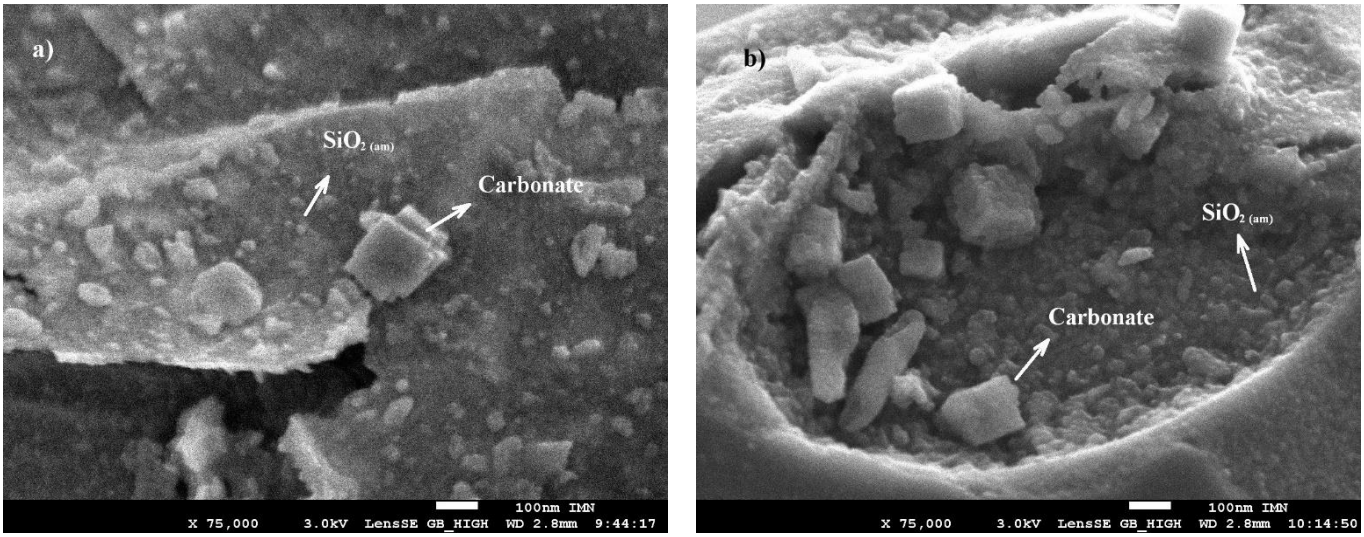

Figure S-5 FG-SEM images of Fo_{65}-olivine reacted sample.

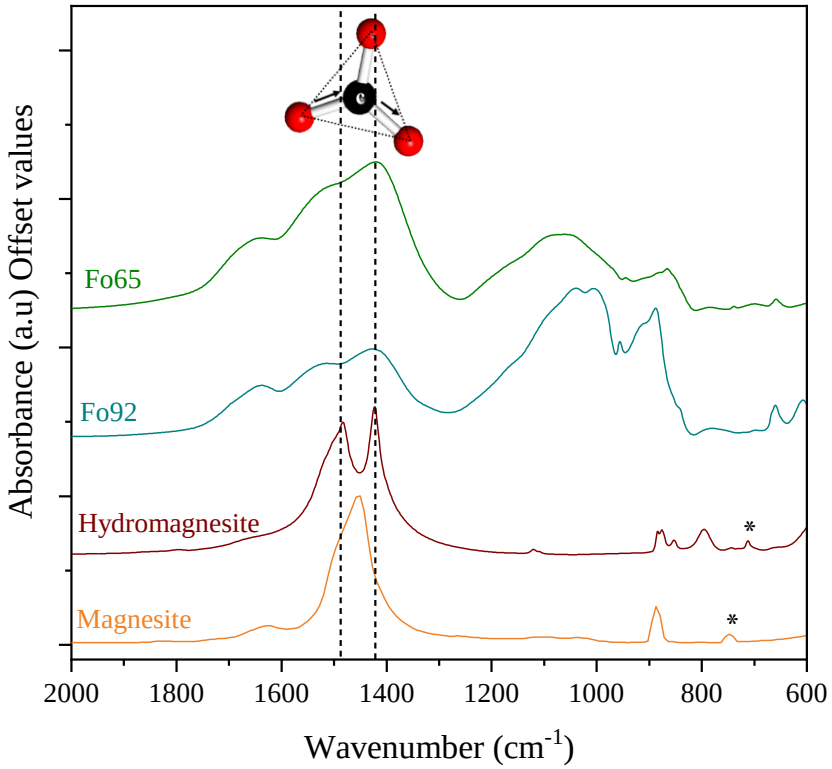

Figure S-6 IR-spectra in the 2000-600 cm^{-1} region of the finest fraction (particle size < 1 µm) of olivine-weathered samples (Fo_{65} and Fo_{92}) on the top and, hydromagnesite and magnesite spectra on the bottom for comparison (from HR inorganics Thermo Fisher database). The split band of asymmetric stretching bands of carbonates ($v_3(CO_3)^{2-}$) matches better with hydromagnesite (dashed lines) than with the magnesite spectrum. The asterisks mark the symmetric band $v_4(CO_3)^{2-}$, which only appears in crystalline carbonate (Gago-Duport *et al.*, 2008).

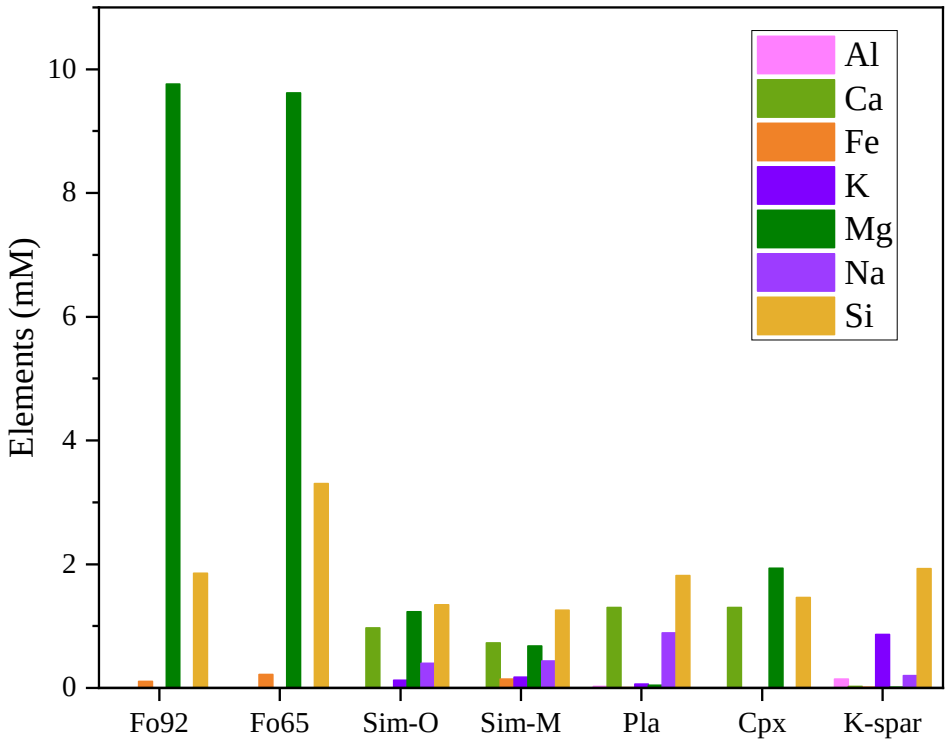

Figure S-7 The fluid chemistry of the samples: magnesium forsterite (Fo_{92}); ferroan forsterite (Fo_{65}), simulant with olivine (Sim-O); simulant with mangnetite (Sim-M); plagioclase (Pla); clinopyroxene (Cpx); K-feldspar (K-spar). They were analysed by Baron *et al.* (2019) using inductively coupled plasma atomic emission spectroscopy (ICP-AES).

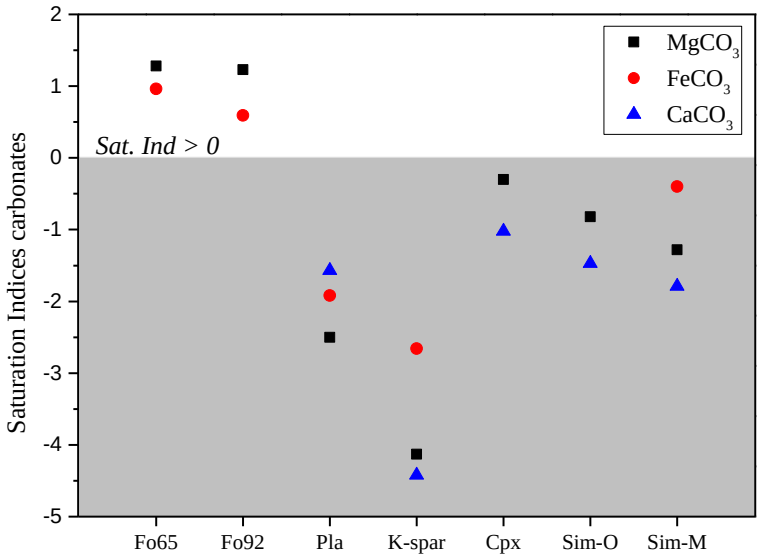

Figure S-8 Mineral saturation indices of carbonates were calculated by Baron *et al.* (2019) with the Phreeqc software and the Thermoddem database. The Eh-pH predominance diagrams of iron solutions showed that olivine reacted samples yielded oxidising conditions that inhibit the formation of siderite.

➢ Geochemical Modelling and Carbonates

The geochemical models considering equilibrium conditions might lead to some uncertainties about the secondary products formed. In these models, a mineral phase can instantaneously precipitate or dissolve, depending on its saturation index (SI), Equation S-1:

$$SI = \log\left(\frac{IAP}{K_{sp}}\right) \qquad \text{Eq. S-1}$$

Being IAP, the ionic activity product of the chemical species, and K_{sp} the solubility product of the mineral. Accordingly, SI>0 indicates mineral precipitation, and SI<0, mineral dissolution.

However, equilibrium calculations are usually biased by the mineral assemblage chosen in the input file, having a significant impact on the model results (Dethlefsen *et al.*, 2012). Additionally, previous studies with batch reactor experiments have shown a strong coupling between mineral dissolution/precipitation kinetic reactions, and consequently, equilibrium conditions were not attainted (Zhu and Lu, 2009; Lu *et al.*, 2013). In this regard, it is important to mention the role of metastable phases, usually not considered in equilibrium models, which are essential to determine the growth of carbonates (Montes-Hernandez and Renard, 2016). Another issue is the effect of secondary ions on the formation of carbonates, such as the well-known inhibition effect of the Mg^{2+} or SO_4^{2-} ions over calcite formation (*e.g.*, Nielsen *et al.*, 2016).

More challenging is to adapt the macroscopic rate laws (*i.e.* that are based upon the chemical affinity of bulk experiments) to incorporate surface microscopic processes (Teng *et al.*, 2000), including the dependence on the degree of supersaturation to overcome the nucleation processes and begin crystal growth (Jiang and Tosca, 2020; Kissick *et al.*, 2021).

For these reasons, geochemical models from basalt dissolution on early Mars might overestimate the carbonate formation. Thus, more laboratory experiments are necessary to refine geochemical models and adjust kinetic rates.

Supplementary Information References

Agee, C.B., Wilson, N.V., McCubbin, F.M., Ziegler, K., Polyak, V.J., Sharp, Z.D., Asmerom, Y., Nunn, M.H., Shaheen, R., Thiemens, M.H., Steele, A., Fogel, M.L., Bowden, R., Glamoclija, M., Zhang, Z., Elardo, S.M. (2013) Unique Meteorite from Early Amazonian Mars: Water-Rich Basaltic Breccia Northwest Africa 7034. *Science* 339, 780-785. https://doi.org/10.1126/science.1228858

Baron, F., Gaudin, A., Lorand, J.-P., Mangold, N. (2019) New Constraints on Early Mars Weathering Conditions From an Experimental Approach on Crust Simulants. *Journal of Geophysical Research: Planets* 124, 1783-1801. https://doi.org/10.1029/2019JE005920

Cánneva, A., Giordana, I.S., Erra, G., Calvo, A. (2017) Organic Matter Characterization of Shale Rock by X-ray Photoelectron Spectroscopy: Adventitious Carbon Contamination and Radiation Damage. *Energy & Fuels 31*, 10414-10419. https://doi.org/10.1021/acs.energyfuels.7b01143

Dethlefsen, F., Haase, C., Ebert, M., Dahmke, A. (2012) Uncertainties of geochemical modeling during CO2 sequestration applying batch equilibrium calculations. *Environmental Earth Sciences* 65, 1105-1117. https://doi.org/10.1007/s12665-011-1360-x

Fairley, N., Fernandez, V., Richard-Plouet, M., Guillot-Deudon, C., Walton, J., Smith, E., Flahaut, D., Greiner, M., Biesinger, M., Tougaard, S., Morgan, D., Baltrusaitis, J. (2021) Systematic and collaborative approach to problem solving using X-ray photoelectron spectroscopy. *Applied Surface Science Advances* 5, 100112. https://doi.org/10.1016/j.apsadv.2021.100112

Gago-Duport, L., Briones, M., Rodríguez, J.B., Covelo, B. (2008) Amorphous calcium carbonate biomineralization in the earthworm's calciferous gland: Pathways to the formation of crystalline phases. *Journal of Structural Biology* 162, 422-435. https://doi.org/10.1016/j.jsb.2008.02.007

Hewins, R.H., Zanda, B., Humayun, M., Nemchin, A., Lorand, J.-P., Pont, S., Deldicque, D., Bellucci, J.J., Beck, P., Leroux, H., Marinova, M., Remusat, L., Göpel, C., Lewin, E., Grange, M., Kennedy, A., Whitehouse, M.J. (2017) Regolith breccia Northwest Africa 7533: Mineralogy and petrology with implications for early Mars. *Meteoritics & Planetary Science* 52, 89-124. https://doi.org/10.1111/maps.12740

Humayun, M., Nemchin, A., Zanda, B., Hewins, R.H., Grange, M., Kennedy, A., Lorand, J.P., Göpel, C., Fieni, C., Pont, S., Deldicque, D. (2013) Origin and age of the earliest Martian crust from meteorite NWA 7533. *Nature* 503, 513-516. https://doi.org/10.1038/nature12764

Jiang, C.Z., Tosca, N.J. (2020) Growth kinetics of siderite at 298.15 K and 1 bar. *Geochimica et Cosmochimica Acta* 274, 97-117. https://doi.org/10.1016/j.gca.2020.01.047

Jones, G.C., Jackson, B. (1993) Infrared Transmission Spectra of Carbonate Minerals. Springer, Dordrecht. https://doi.org/10.1007/978-94-011-2120-0

Kissick, L.E., Mather, T.A., Tosca, N.J. (2021) Unravelling surface and subsurface carbon sinks within the early Martian crust. *Earth and Planetary Science Letters* 557, 116663. https://doi.org/10.1016/j.epsl.2020.116663

Kloprogge, T., Wood, B. (2020) Handbook of Mineral Spectroscopy Volume 1 X-ray Photoelectron Spectra. In: Kloprogge, J.T. and Wood, B.J. (Eds.) Elsevier, Amsterdam (Netherlands), Oxford (UK), Cambridge (USA). https://doi.org/10.1016/B978-0-12-804522-0.00001-8

Le Bas, M.J., Le Maitre, R.W., Streckeisen, A., Zanettin, B. (1986) A Chemical Classification of Volcanic Rocks Based on the Total Alkali-Silica Diagram. *Journal of Petrology* 27, 745-750. https://doi.org/10.1093/petrology/27.3.745

Lu, P., Fu, Q., Seyfried, W.E., Hedges, S.W., Soong, Y., Jones, K., Zhu, C. (2013) Coupled alkali feldspar dissolution and secondary mineral precipitation in batch systems – 2: New experiments with supercritical CO2 and implications for carbon sequestration. *Applied Geochemistry* 30, 75-90. https://doi.org/10.1016/j.apgeochem.2012.04.005

Mangold, N., Thompson, L.M., Forni, O., Williams, A.J., Fabre, C., Le Deit, L., Wiens, R.C., Williams, R., Anderson, R.B., Blaney, D.L., Calef, F., Cousin, A., Clegg, S.M., Dromart, G., Dietrich, W.E., Edgett, K.S., Fisk, M.R., Gasnault, O., Gellert, R., Grotzinger, J.P., Kah, L., Le Mouélic, S., McLennan, S.M., Maurice, S., Meslin, P.-Y., Newsom, H.E., Palucis, M.C., Rapin, W., Sautter, V., Siebach, K.L., Stack, K., Sumner, D., Yingst, A. (2016) Composition of conglomerates analyzed by the Curiosity rover: Implications for Gale Crater crust and sediment sources. *Journal of Geophysical Research: Planets* 121, 353-387. https://doi.org/10.1002/2015JE004977

Montes-Hernandez, G., Renard, F. (2016) Time-Resolved in Situ Raman Spectroscopy of the Nucleation and Growth of Siderite, Magnesite, and Calcite and Their Precursors. *Crystal Growth & Design* 16, 7218-7230. https://doi.org/10.1021/acs.cgd.6b01406

Morrison, S.M., Downs, R.T., Blake, D.F., Vaniman, D.T., Ming, D.W., Hazen, R.M., Treiman, A.H., Achilles, C.N., Yen, A.S., Morris, R.V., Rampe, E.B., Bristow, T.F., Chipera, S.J., Sarrazin, P.C., Gellert, R., Fendrich, K.V., Morookian, J.M., Farmer, J.D., Des Marais, D.J., Craig, P.I. (2018) Crystal chemistry of martian minerals from Bradbury Landing through Naukluft Plateau, Gale crater, Mars. *American Mineralogist* 103, 857-871. https://doi.org/10.2138/am-2018-6124

Nielsen, M.R., Sand, K.K., Rodriguez-Blanco, J.D., Bovet, N., Generosi, J., Dalby, K.N., Stipp, S.L.S. (2016) Inhibition of Calcite Growth: Combined Effects of Mg2+ and SO42–. *Crystal Growth & Design* 16, 6199-6207. https://doi.org/10.1021/acs.cgd.6b00536

Parkhurst, D.L., Apello, C.A. (2014) Description of Input and Examples for Phreeqc Version 3: A Computer Program for Speciation, Batch-reaction, One-dimensional Transport, and Inverse Geochemical Calculations. *Techniques and Methods*, Reston, VA. https://doi.org/10.3133/tm6A43

Payne, B.P., Biesinger, M.C., McIntyre, N.S. (2011) X-ray photoelectron spectroscopy studies of reactions on chromium metal and chromium oxide surfaces. *Journal of Electron Spectroscopy and Related Phenomena* 184, 29-37. https://doi.org/10.1016/j.elspec.2010.12.001

Teng, H.H., Dove, P.M., De Yoreo, J.J. (2000) Kinetics of calcite growth: surface processes and relationships to macroscopic rate laws. *Geochimica et Cosmochimica Acta* 64, 2255-2266. https://doi.org/10.1016/S0016-7037(00)00341-0

Zhu, C., Lu, P. (2009) Alkali feldspar dissolution and secondary mineral precipitation in batch systems: 3. Saturation states of product minerals and reaction paths. *Geochimica et Cosmochimica Acta* 73, 3171-3200. https://doi.org/10.1016/j.gca.2009.03.015